ADVANCING EARTH AND SPACE SCIENCES

JGR Atmospheres

RESEARCH ARTICLE
10.1029/2024JD041173

Key Points:

- Local (remote) effects of the sub-grid turbulent orographic form drag (STOFD) affect precipitation in the Southeastern (Northern) China
- Remote effects of the STOFD strongly affect the atmospheric circulation and improve the precipitation simulation in the Northern China
- Local effects of the STOFD can enhance the precipitation in the Southeastern China by generating more concentrated disturbances

Correspondence to:
A. Huang,
anhuang@nju.edu.cn

Citation:
Zhou, Y., Huang, A., Li, X., Gu, C., & Wu, Y. (2024). Local and remote effects of the sub-grid turbulent orographic form drag on the summer monsoon precipitation over Eastern China. *Journal of Geophysical Research: Atmospheres*, *129*, e2024JD041173. https://doi.org/10.1029/2024JD041173

Received 11 MAR 2024
Accepted 8 OCT 2024

Author Contributions:
Conceptualization: Anning Huang
Data curation: Yuchen Zhou, Chunlei Gu
Formal analysis: Yuchen Zhou, Yang Wu
Investigation: Yuchen Zhou, Xin Li, Yang Wu
Methodology: Yuchen Zhou, Anning Huang, Xin Li, Chunlei Gu
Resources: Yuchen Zhou, Chunlei Gu, Yang Wu
Software: Yuchen Zhou, Chunlei Gu
Supervision: Anning Huang
Validation: Yuchen Zhou
Visualization: Yuchen Zhou
Writing – original draft: Yuchen Zhou, Anning Huang, Xin Li
Writing – review & editing: Anning Huang, Xin Li, Yang Wu

Local and Remote Effects of the Sub-Grid Turbulent Orographic Form Drag on the Summer Monsoon Precipitation Over Eastern China

Yuchen Zhou[1], Anning Huang[1,2], Xin Li[3], Chunlei Gu[1], and Yang Wu[3]

[1]School of Atmospheric Sciences, Nanjing University, Nanjing, China, [2]Qinghai Lake Comprehensive Observation Research Station, Chinese Academy of Sciences, Gangcha, China, [3]Key Laboratory of Transportation Meteorology of China Meteorological Administration, Nanjing Joint Institute for Atmospheric Sciences, Nanjing, China

Abstract The sub-grid turbulent orographic form drag (STOFD) significantly affects the regional circulation and precipitation. This study explores the local and remote effects of the STOFD on the summer monsoon precipitation across Eastern China using the Regional Climate Model Version 4 adopting a STOFD scheme. Results indicate that the local and remote effects of the STOFD primarily influence the improvement of summer precipitation simulation in the Southeastern and Northern China, respectively. The local effects of the STOFD can lead to 37.1% and 10.7% reduction of the absolute error and the root mean square error (RMSE) of simulated summer precipitation in the Southeastern China with complex sub-grid terrains. The remote effects of the STOFD within the Indochina Peninsula and Yunnan-Guizhou Plateau result in the absolute error and RMSE of simulated summer precipitation in the Northern China with mild sub-grid terrain decreased by 90.1% and 32.9%, respectively. Moreover, the remote effects of the STOFD within the Tianshan Mountains and Tibetan Plateau can clearly improve the simulated precipitation in both the Southeastern and Northern China. The disturbances generated by the local effects of the STOFD are more locally concentrated than those produced by the STOFD remote effects, leading to a more significant improvement of precipitation simulation in the Southeastern China. While the disturbances resulted from the remote effects of the STOFD affect the summer precipitation in both the Southeastern and Northern China obviously. This study highlights the significance of the remote effects of the STOFD in improving the summer precipitation simulation in Eastern China.

Plain Language Summary Due to resolution limitations, micro-scale terrains are often ignored in climate simulations. While the collision between airflow and sub-grid micro-scale terrains produces turbulence, which results in sub-grid turbulent orographic form drag (STOFD). A STOFD scheme has been applied in the Regional Climate Model and proved its ability to improve the summer precipitation simulation in Eastern China. However, the specific source of the improvements remains unclear. This study explores the local and remote effects of the STOFD on precipitation simulation and reveals possible mechanisms. Results show that the remote effects of the STOFD greatly improve the precipitation simulation in the Northern China with mild sub-grid terrains by inducing substantial disruptions in atmospheric circulation and related factors. Whereas both the local and remote effects of the STOFD significantly affect the precipitation simulation in the Southeastern China with complex sub-grid terrains. This research emphasizes the crucial role of the remote effects of the STOFD.

1. Introduction

The East Asian summer monsoon (EASM), which impacts a quarter of the global population, is influenced by a combination of tropical and mid-latitude factors (Chen & Bordoni, 2014; Ding & Chan, 2005; Wu et al., 2009). The summer precipitation with increased variability over Eastern China is predominantly controlled by the EASM (Ding, 1992; Sanders, 1988; Tao et al., 2004). The increased variability in precipitation leads to frequent occurrences of both droughts and floods, which significantly affect social and economic development (Huang et al., 2007; Ye & Lu, 2012; Zheng et al., 2006). Therefore, it is crucial to explore the factors that influence summer monsoon precipitation in Eastern China to improve the prediction accuracy.

The EASM is influenced by various factors on multiple time scales, including anomalies in sea surface temperature, snow cover, the Indian summer monsoon, and others (Chen et al., 2019; Jin & Huo, 2018; S. Li et al., 2023; Wei et al., 2014; Yim et al., 2010). Different types of El Niño-Southern Oscillation events, along with their developmental stages, can alter the position and intensity of the Western Pacific Subtropical High, subsequently affecting the EASM (Ronghui & Yifang, 1989; Weng et al., 2007). Additionally, the anomaly of winter snow cover on the Tibetan Plateau (TP) can impact the EASM by altering the land-sea thermal contrast or the Philippine Sea anticyclone in June (Ren et al., 2016).

Furthermore, terrain across various scales plays a crucial role in shaping EASM. Large-scale topography influences the related atmospheric circulation through both dynamic and thermodynamic effects (Lu et al., 2021; Wu et al., 2014). The static Rossby waves generated by TP produce a downstream zonal pressure gradient and southerly winds, which affect the water vapor transport in the EASM (Son et al., 2020). The intense heating over TP enhances the downstream southwesterly wind circulation and promotes the convergent upward movement of water vapor, leading to the early onset of EASM (Duan et al., 2020). Furthermore, the micro- and mesoscale topography can create dynamic and thermal disturbances that spread and affect the EASM precipitation (Duan et al., 2012; Grabowski, 1989; Shi et al., 2008).

Numerical models have been widely employed to explore the impact of terrain and other key factors on weather and climate. Previous studies directly remove, smooth, or add terrain and related variables to visualize the weather and climate effects of the terrain across various scales (Babaei et al., 2021; J. Li et al., 2023; Pontoppidan et al., 2017; Wang et al., 2020; Wu et al., 2016; Xu et al., 2024). A large part of these studies is based on several years or just a major event of simulations to demonstrate the impact of topography on climate, so it is reasonable to assume that the average of several-year simulation is sufficient to represent regional climate (Babaei et al., 2021; Pontoppidan et al., 2017; Wang et al., 2020; Wu et al., 2016; Xu et al., 2024). Among these terrain effects, the micro-scale topography with horizontal scales less than 5 km can generate sub-grid turbulent orographic form drag (STOFD, Beljaars et al., 2004; Koo et al., 2018; Zhou et al., 2019; Zhou, Yang, & Wang, 2017). The amount of stress caused by the STOFD is equal to or even greater than that caused by the land cover frictions (Belcher & Wood, 1996; Xue et al., 2011).

Solely increasing the model resolution cannot enhance the representation of the STOFD. Wood et al. (2001) proposed a scheme for directly parameterizing STOFD, and several related schemes were then developed on the conception of this scheme (Beljaars et al., 2004; Jiménez & Dudhia, 2012; Rontu, 2006). These schemes have been successfully applied and validated in several numerical models, demonstrating the positive impacts of the STOFD on the model performance (Beljaars et al., 2004; Liang et al., 2017; Milton & Wilson, 1996; Zhou, Yang, & Wang, 2017). For instance, Zhou et al. (2019) compared two topographic turbulent drag schemes and found that the STOFD scheme proposed by Beljaars et al. (2004) leads to a more obvious improvement of atmospheric circulation simulation. The STOFD scheme reduces more than 7% and 5% of the seasonal root mean square error (RMSE) and deviation in the simulated surface winds in the Southeastern China, respectively (Xue et al., 2021).

While existing researches have primarily focused on the local effects of the STOFD at the synoptic scale, the remote effects of the STOFD and the relative roles of the local and remote effects of the STOFD at the climate scale receive little attention (Lim et al., 2019; Matsukawa et al., 2022; Xue et al., 2021; Xue & Shen, 2023). However, the remote climatic effect of terrains, as mediated by airflow, cannot be overlooked (Blumen, 1988; Duine et al., 2021; Lane & Watson, 2012; Xu et al., 2024). For instance, the EASM exhibits a distinct seasonal rainfall migration, which is different from other monsoon systems due to the remote influence of TP (Chiang et al., 2020; Seok & Seo, 2021). Additionally, the Tianshan Mountains, Yunnan-Guizhou Plateau, and Indochina Peninsula also have remote effects on the Asian monsoon by modifying the atmospheric circulation (Baldwin & Vecchi, 2016; Shi et al., 2017; Zhuang et al., 2022). Recently, Gu et al. (2023b) integrated the STOFD scheme (Beljaars et al., 2004) into the Regional Climate Model Version 4 (RegCM4) and found that adopting the STOFD scheme can reduce the RMSE of the 10-year average simulated summer precipitation by up to 30% over Eastern China. This significant improvement is mainly attributed to the remote effects of the STOFD, while a quantitative analysis of the local and remote effects of the STOFD and their relative importance has not been provided yet.

Previous studies have underscored the notable impacts of STOFD on local circulation and precipitation, and some of them also highlighted the importance of the remote effects of the STOFD (Gu et al., 2023b; Lim et al., 2019; Matsukawa et al., 2022; Xue et al., 2021; Xue & Shen, 2023). Nonetheless, the remote effects of the STOFD have been less explored and warrant further research. To delve deeper into the impacts of the local and remote effects of the STOFD on the summer precipitation simulation in Eastern China, we use the RegCM4 adopting the STOFD scheme (Gu et al., 2023b) to conduct sensitivity experiments. These experiments activate the STOFD scheme in different sub-regions independently, enabling us to quantify the relative contributions of the local and remote effects of the STOFD on the summer precipitation simulation over Eastern China and enhance our understanding of the associated physical mechanisms.

This paper not only reveals the influence of remote effects of the STOFD on precipitation quantitatively but also conducts a comparative analysis with the local effects of the STOFD. It further explores the differences in the influence mechanism of the local and remote effects of the STOFD on precipitation. The remaining parts of this paper are arranged as follows: Section 2 introduces the model, data, metrics and experimental design. Section 3 systematically shows the influence of local and remote effects of the STOFD on the summer precipitation in Eastern China. Section 4 explores the underlying physical mechanisms. The conclusion and discussion can be found in Section 5.

2. Model, Data, Methodology and Experimental Design

2.1. RegCM4 Model With the STOFD Scheme

The RegCM4, developed from the first limited area model designed for long-term regional climate simulation, has gained popularity in a wide range of regional climate studies (Ashfaq et al., 2021; Giorgi, 2019; Giorgi et al., 2012; Raju et al., 2015; Shalaby et al., 2012). The RegCM4 with high resolution provides detailed regional climate assessments of complex terrain regions, with preferable representations of physical mechanisms (Berg et al., 2013; Giorgi, 2019). The RegCM4 is one of the most commonly used regional climate models in East Asia (Gao & Giorgi, 2017). Although a new version (RegCM5) is available, RegCM4 is used in this paper because the performance of RegCM4 is comprehensively evaluated over Eastern China (Gao et al., 2017; Xu et al., 2022).

The STOFD scheme developed by Beljaars et al. (2004) was incorporated into the RegCM4 (Gu et al., 2023b) to improve the ability to describe the sub-grid terrain dynamic effects. The STOFD at each level of atmosphere is calculated by:

$$\frac{\partial}{\partial z}\left(\frac{\tau_0}{\rho}\right) = -1.08372058 \times 10^{-7} \cdot \left|\vec{V}\right| \cdot \vec{V} \cdot e^{-\left(\frac{z}{1500}\right)^{1.5}} \cdot \sigma_{flt}^{2} \cdot z^{-1.2} \tag{1}$$

where z, τ_0 and ρ represent the elevation of the level above the ground surface (unit: m), wind stress (unit: $\mathrm{N \cdot m^{-2}}$), and air density (unit: $\mathrm{kg \cdot m^{-3}}$) at each model grid, respectively. $\vec{V}$ is the horizontal wind (unit: $\mathrm{m \cdot s^{-1}}$). σ_{flt} is the standard deviation of filtered sub-grid terrain height (unit: m), and the filtering method is introduced by Beljaars et al. (2004). This scheme introduces a resistance that decays exponentially with increasing elevation at each level. It has been widely acknowledged for its ability to accurately represent the STOFD and shown superior performance than other STOFD schemes in improving the climate model simulations (Wang et al., 2020; Xue et al., 2021; Zhou et al., 2017a, 2019). Specifically, the STOFD scheme can significantly enhance RegCM4's ability to simulate the summer precipitation over Eastern China (Gu et al., 2023b).

The experiments are conducted by the RegCM4 model adopting the STOFD scheme with a 25 km horizontal resolution and 23 vertical layers extending from the surface up to 50 hPa. The domain is shown in Figure 1, centered at (34°N, 107°E), consisting of 320 and 240 grids in zonal and meridional directions, respectively. The details of the experimental design are shown in Section 2.3.

2.2. Data

The atmospheric initial and lateral boundary conditions of the RegCM4 model are provided by the 1.5° × 1.5° ERA-Interim Reanalysis (EIN15) with the temporal resolution of 6 hr (Dee et al., 2011). The oceanic surface conditions are derived from the 1° × 1° Optimum Interpolation Sea Surface Temperature (OISST) data provided by the National Oceanic and Atmospheric Administration (NOAA, Reynolds et al., 2002). The initial conditions of the land surface model are derived from the 0.25° × 0.25° European Space Agency (ESA) Climate Change Initiative (CCI) Essential Climate Variable (ECV) surface soil moisture and combined product (Dorigo et al., 2021).

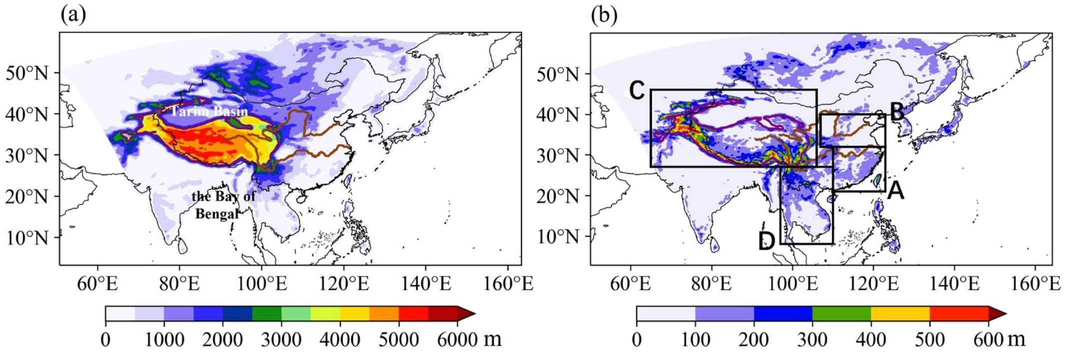

Figure 1. The elevation (a) and standard deviation of the filtered elevation (b) across the model domain. The black rectangles marked with A, B, C, and D indicate the areas where the sub-grid turbulent orographic form drag (STOFD) scheme is activated in the experiments of SEC_exp, NC_exp, TS_TP_exp, and IP_YG_exp, respectively. The full plotting domain indicates the model domain and the area where the STOFD is activated in the All_exp experiment. The purple contour lines represent the elevation of 3,000 m. The brown lines depict the Yangtze River and Yellow River.

Three types of data are used for model evaluation.

1. The daily Asian Precipitation-Highly-Resolved Observational Data Integration Toward Evaluation (APHRODITE) grid precipitation with a 0.25° × 0.25° horizontal resolution in the summers (June to August) of 2011–2015 (Yatagai et al., 2012). It is based on a dense rain-gauge data network in Asia.
2. The fifth generation of European Reanalysis (ERA5, Hersbach et al., 2020) atmospheric reanalysis of the global climate produced by European Centre for Medium-Range Weather Forecasts, covering the period from January 1940 to present with a horizontal resolution of 0.25° × 0.25° and temporal resolution of 1 hr, providing the air pressure, relative humidity, specific humidity, vertical velocity, and wind field at different levels in the summers of 2011–2015.
3. The enhanced global data set for the land component of the ERA5 (ERA5-Land Muñoz-Sabater, 2019) covering the period from January 1950 to present, boasting a fine horizontal resolution of 0.1° × 0.1° and temporal resolution of 1 hr, offering information on the 10 m wind during the summer of 2011–2015.

2.3. Methodology and Experimental Design

The summer mean daily precipitation of the simulations and observation, and the Root Mean Squared Error (RMSE) of the daily precipitation simulations in summer based on the observed data are used to assess the model performance and the remote and local impact of STOFD of key regions. All significant differences in this study are determined by the Student's *t*-test (Student, 1908).

The σ_{flt} is the sole input for the calculation of STOFD. By setting the value of σ_{flt}, we can accurately capture the dynamic impacts of micro-scale topography in simulations. This scheme allows for selective activation in different sub-regions by assigning a σ_{flt} value of 0 in other regions, facilitating to explore the influence of STOFD of the sub-regions. In this study, the σ_{flt} is calculated using the 30″ × 30″ (~1 km × ~1 km) Global Multi-resolution Terrain Elevation Data (GMTE, Danielson & Gesch, 2011) following Beljaars et al. (2004) and Xue et al. (2021). The GMTE data also provide the grid-scale elevation (Figure 1a).

Higher σ_{flt} indicates that the sub-grid terrain is more complex. In Eastern China, the Southeastern China (21–32°N, 110–123°E, rectangle A) shows relatively higher σ_{flt}, while the Northern China (32–40°N, 107–123°E, rectangle B) displays a much lower σ_{flt} (Figure 1b). Therefore, the Southeastern China with complex sub-grid terrain and the Northern China with mild sub-grid terrain are chosen as the key regions to evaluate the improvement of precipitation simulation in the areas with different local sub-grid terrain complexity. Previous studies have shown that the large-scale and mesoscale terrains of the TP, Tianshan Mountains, Yunnan-Guizhou Plateau, and Indochina Peninsula induce significant remote effects on the Asian monsoon (Baldwin & Vecchi, 2016; Shi et al., 2017; Zhuang et al., 2022). In addition, the Tianshan Mountains and TP (27–46°N, 65–106°E, rectangle C) and the Indochina Peninsula and Yunnan-Guizhou Plateau (8–27°N, 97–110°E, rectangle D) are in a critical region where the westerly and southwest flows pass respectively and both have relatively higher σ_{flt}. Therefore, the remote effects of the STOFD in these regions on the precipitation of EASM are worth to be

Table 1
Experimental Design

Experiments	The region where the STOFD scheme is enabled	Experimental purpose
CTRL	No STOFD scheme enabled	Control experiment
All_exp	Full domain (Figure 1b)	Confirm the total influence of STOFD in the model domain
SEC_exp	Southeastern China (21–32°N, 110–123°E), label A in Figure 1b	Explore the local effect of STOFD of the regions with complex sub-grid terrain
NC_exp	Northern China (32–40°N, 107–123°E), label B in Figure 1b	Explore the local effect of STOFD of the regions with mild sub-grid terrain
TS_TP_exp	Tianshan Mountains and Tibetan Plateau (27–46°N, 65–106°E), label C in Figure 1b	Explore the remote effect of STOFD
IP_YG_exp	Indochina Peninsula and Yunnan-Guizhou Plateau (8–27°N, 97–110°E), label D in Figure 1b	Explore the remote effect of STOFD

explored. This study aims to explore the remote effects of the STOFD generated by micro-scale topography in the regions mentioned above and compare it with the local effects.

A control experiment (CTRL) and four sensitivity experiments named SEC_exp, NC_exp, TS_TP_exp, and IP_YG_exp are conducted to explore the local and remote effects of the STOFD. The STOFD scheme is individually enabled in the Southeastern China, the Northern China, the Tianshan Mountains and TP, and the Indochina Peninsula and Yunnan-Guizhou Plateau in the SEC_exp, NC_exp, TS_TP_exp, and IP_YG_exp experiments, respectively. The STOFD scheme is disabled in the CTRL experiment. Also, an experiment labeled as All_exp, in which the STOFD scheme is enabled over the entire model domain, is conducted to confirm the total influence of STOFD in the model domain on the summer precipitation simulation in Eastern China. The subregions in which the STOFD is activated are outlined by black rectangles in Figure 1b. The details of the experimental design are shown in Table 1.

The only difference between these experiments is the different regions where the STOFD scheme is enabled. The other settings of these experiments are totally identical. The hydrostatic dynamic core is adopted with the domain center located at (34°N, 107°E), with a grid of 320 and 240 grids in zonal and meridional directions, respectively. The horizontal resolution is set to 25 km. The model has 23 vertical layers and extends from the surface up to 50 hPa. The simulation covers the period from 1 May to 31 August for each year from 2011 to 2015, with the month of May being designated as the model spin-up period. The output data for the period from 1 June to 31 August are analyzed to explore effects of the STOFD. The time step is 30 s, and the model outputs are generated every 24 hr. The calculations for long-wave radiation absorption-emission of cloud and gas particles, convection, land surface process, and solar radiation are performed every hour, 30 s, 10 min, and 10 min, respectively. The lateral boundary conditions of the atmosphere are derived from the EIN15 data with a time resolution of 6 hr.

The Tiedtke cumulus scheme (Tiedtke, 1996) and the Kain-Fritsch cumulus scheme (Kain & Fritsch, 1990) are employed over the land and ocean, respectively. The Zeng ocean flux scheme (Zeng et al., 1998), the Community Land Model version 4.5 (CLM4.5, Oleson et al., 2010), the sub-grid explicit moisture scheme (SUBEX, Pal et al., 2000), the radiation transfer module of the Community Climate Model version 3 (CCM3, Kiehl et al., 1998), and the Holtslag planetary boundary layer scheme (Holtslag et al., 1990) are selected for the simulation.

3. Results

Figures 2a and 2b illustrate that the RegCM4 without the STOFD scheme can generally capture the spatial pattern of summer mean precipitation in Eastern China. However, the simulated rain belt exhibits an obvious northward shift, showing the summer precipitation in the Northern China overestimated by 15.9% and the summer precipitation in the Southeastern China underestimated by 27.6% compared to the observation (Figure 2c). The All_exp experiment with the STOFD scheme activated over the entire model domain can clearly reduce the biases of summer precipitation simulation in the Southeastern China and Northern China compared to the CTRL experiment without the STOFD scheme (Figures 2d and 2i).

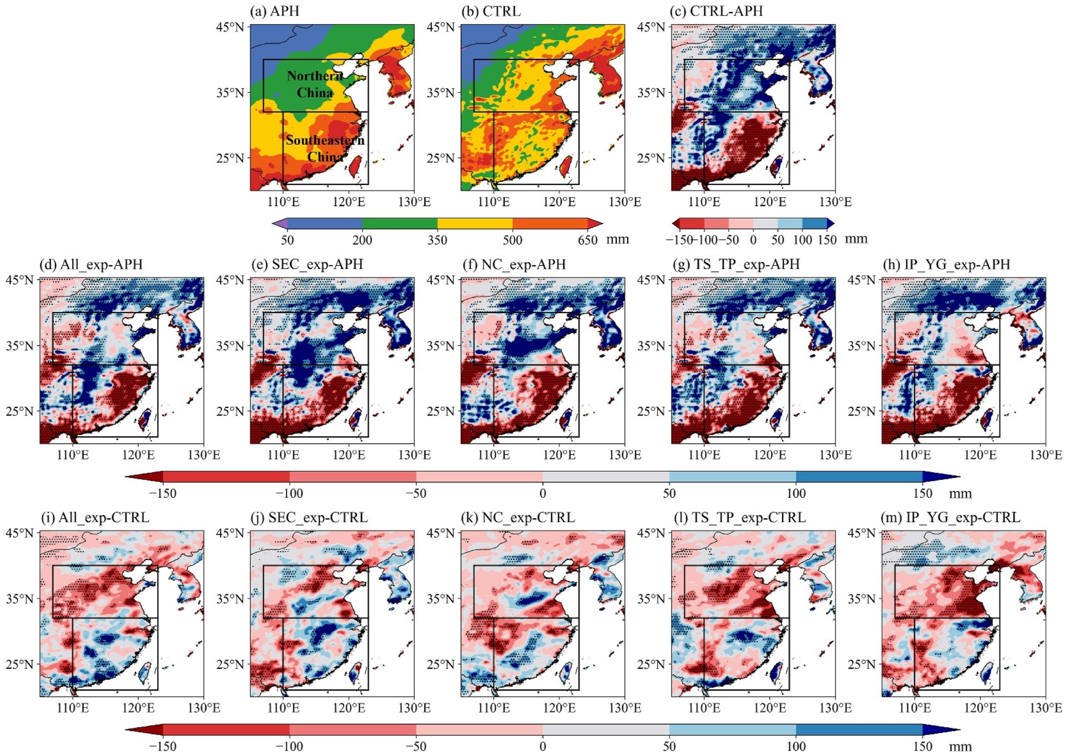

Figure 2. The observed (a) and simulated summer mean precipitation in the CTRL experiment (b), the differences of summer mean precipitation between the CTRL (each sensitivity) experiment and observation (c–h), and the differences of summer mean precipitation between each sensitivity experiment and the CTRL experiment (i–m). The regions of the Southeastern China and Northern China are indicated by the black lines. The differences that pass the 90% significance level are dotted.

Inclusion of the STOFD in different sub-regions can lead to different degrees of improvement in summer precipitation simulation over Eastern China (Figures 2e–2h). These sensitivity experiments produce increased precipitation in the Southeastern China and decreased precipitation in the Northern China to varying extents (Figures 2j–2m). Over the Southeastern China with complex sub-grid terrain, the local effects of the STOFD increase simulated precipitation there (Figure 2j), playing a prominent role in improving the precipitation simulation (Figure 2). The STOFD of the Indochina Peninsula and Yunnan-Guizhou Plateau has the most significant effect on the improvement of precipitation simulation in the Northern China with mild sub-grid terrain (Figures 2h and 2m), followed by the impact of the STOFD over the Tianshan Mountains and TP (Figures 2g and 2l). Whereas the local effects of the STOFD within the Northern China are minimal due to its weaker intensity (Figures 2f and 2k). For the Northern China, the All_exp, TS_TP_exp and IP_YG_exp experiments can well improve the spatial pattern of simulated precipitation (Figures 2d, 2g, 2h, 2i, 2l, and 2m). However, in the Southeastern China, the All_exp and SEC_exp experiments which can clearly improve the precipitation simulation only resulted in a reduction of precipitation simulation bias without fundamentally altering the spatial pattern of precipitation (Figures 2d, 2e, 2i, and 2j).

Figure 3 further shows the summer mean daily precipitation and the RMSE of simulated precipitation to better evaluate the impact of STOFD in different regions on the summer precipitation simulation over Eastern China. As shown in Figure 3a, the summer mean daily precipitation in the Southeastern China simulated by the CTRL experiment is 0.94 mm·d^{-1} less than the observation. Compared to the CTRL experiment, including the impact of STOFD in different regions reduces the absolute error of the summer precipitation simulation in the Southeastern China by varying percentages: the reductions are 48.5% for the All_exp experiment, 37.1% for the SEC_exp experiment, 17.3% for the TS_TP_exp experiment, 8.6% for the IP_YG_exp experiment, and 0.6% for the NC_exp experiment. The All_exp experiment shows the highest reduction of absolute error in precipitation simulation over the Southeastern China among the 5 sensitivity experiments, followed by the SEC_exp and TS_TP_exp experiments. While the local effects of the STOFD within the Southeastern China result in the largest

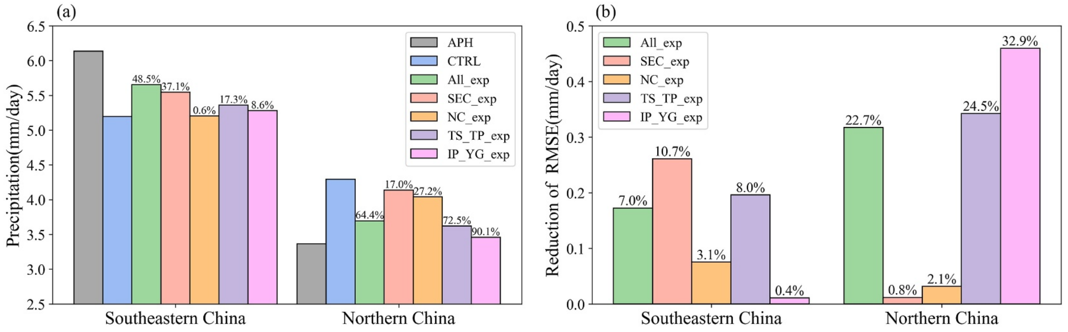

Figure 3. Mean precipitation in summer (a), and the reduction of RMSE in each sensitivity experiment compared to the CTRL experiment (b). The percentages on the bar charts show the relative reduction of absolute error (a) and RMSE (b) of 5-year mean summer precipitation in the Southeastern China and Northern China simulated by each sensitivity experiment relative to the CTRL experiment.

reduction of RMSE of the precipitation simulation over there (Figure 3b). The STOFD in the Southeastern China, Tianshan Mountains and TP, and whole model domain can lead to the RMSE of the simulated precipitation in the Southeastern China decreased by 10.7%, 8.0%, and 7.0% compared to the CTRL experiment, respectively.

The summer mean daily precipitation in the Northern China simulated by the CTRL experiment exceeds the observation by 0.93 mm·d^{-1} (Figure 3a). The improvements of precipitation simulation over the Northern China in the IP_YG_exp experiment are the most significant, followed by the TS_TP_exp experiment, with the absolute error of summer mean precipitation reduced by 90.1% and 72.5%, respectively. Enabling the STOFD scheme in the Indochina Peninsula and Yunnan-Guizhou Plateau, the Tianshan Mountains and TP, the whole model domain, the Northern China, and the Southeastern China can reduce the RMSE of the simulated precipitation in the Northern China by 32.9%, 24.5%, 22.7%, 2.1%, and 0.8% compared to the CTRL experiment, respectively (Figure 3b).

Overall, among the STOFD effects in the four sub-regions, the most significant reductions in the RMSE and absolute error of summer precipitation simulation in the Southeastern China are attributed to the STOFD local effects. While the greatest reductions in the RMSE and absolute error of the summer precipitation simulation in the Northern China are contributed by the remote effects of the STOFD within the Indochina Peninsula and Yunnan-Guizhou Plateau. Unexpectedly, the improvement of the precipitation simulation in the Southeastern and Northern China induced by the STOFD of the whole model domain is less significant than the STOFD of the Southeastern China, Indochina Peninsula and Yunnan-Guizhou Plateau. This indicates that there are additional coincidental factors affecting the simulated precipitation enhancement. The coincidence can be attributed to the imperfect representation of STOFD by the scheme, which fails to account for the impact factors such as boundary-layer stability and interactions of individual orography wave numbers effects (Beljaars et al., 2004; Wood et al., 2001). Additionally, the mutual cancellations of STOFD effects in different sub-regions may play a role in this unexpected result.

To conclude, for the Southeastern China with complex sub-grid terrain, the local effects of the STOFD, as well as the remote effects of the STOFD within the Tianshan Mountains and TP has a considerable impact on precipitation simulation. While the impact of local effects of the STOFD on the precipitation simulation in the Northern China with mild sub-grid terrain is weak. The remote effects of the STOFD within the Indochina Peninsula and Yunnan-Guizhou Plateau, and the Tianshan Mountains and TP significantly mitigate the precipitation overestimation in the Northern China compared to the CTRL experiment. The remote effects of the STOFD within the Tianshan Mountains and TP contributes to the remarkable improvement of precipitation simulation in both the Southeastern and Northern China.

4. Physical Mechanisms

Since this study mainly explores the local and remote effects of the STOFD in different sub-regions, only the impact mechanisms related to the STOFD of each sub-region are introduced below. Compared to the CTRL experiment, the effects of STOFD within the Southeastern China, Tianshan Mountains and TP, and Indochina

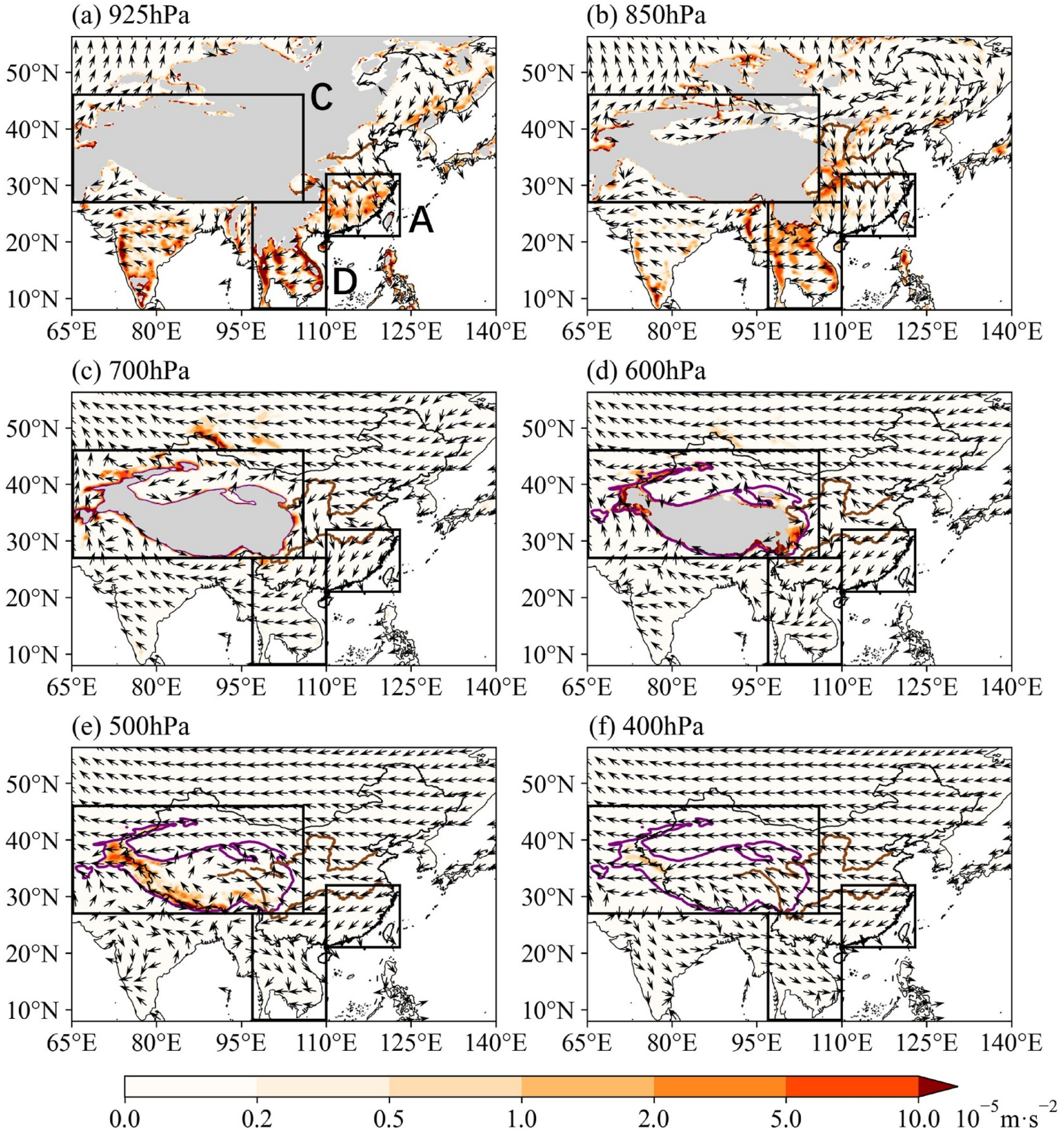

Figure 4. The direction (arrows) and magnitude (color shadings, units: 10^{-5}m·s^{-2}) of sub-grid turbulent orographic form drag (STOFD) at different levels in the ALL_exp experiment. The arrows and color shadings are tendencies in the momentum equations of the STOFD scheme. The black rectangles marked with A, C, and D indicate the direction (arrows) and magnitude (color shadings) of STOFD in the SEC_exp, TS_TP_exp, and IP_YG_exp, respectively. The gray shadow indicates the terrain height is higher than the altitude of the air pressure level. The purple contour lines represent the elevation of 3,000 m. The brown lines depict the Yangtze River and Yellow River.

Peninsula and Yunnan-Guizhou Plateau significantly reduced the absolute error and RMSE of simulated precipitation in the Southeastern and Northern China (Figure 3). The mechanisms related to the effects of the STOFD in these three regions will be explored below in detail.

The STOFD opposing the wind direction extends from the surface to 400 hPa with different magnitudes and directions at different levels. The STOFD at 6 representative levels has been highlighted in Figure 4. In the SEC_exp experiment, the STOFD at 925 hPa is particularly prominent, exerting a strong southward force (Figure 4a, rectangle A). At 850 hPa, the force diminishes but still maintains a southward direction (Figure 4b, rectangle A). The sub-grid topography of the Tianshan Mountains and TP is highly complex, with the STOFD of this region mainly occurring in the mid-level troposphere with large magnitude (Figures 4c–4e, rectangle C). From 600 to 400 hPa, the STOFD along the northern side of TP is acting westward predominantly (Figures 4d–4f, rectangle C). While in the other areas, it exhibits chaotic directions. In the lower troposphere over the Tianshan

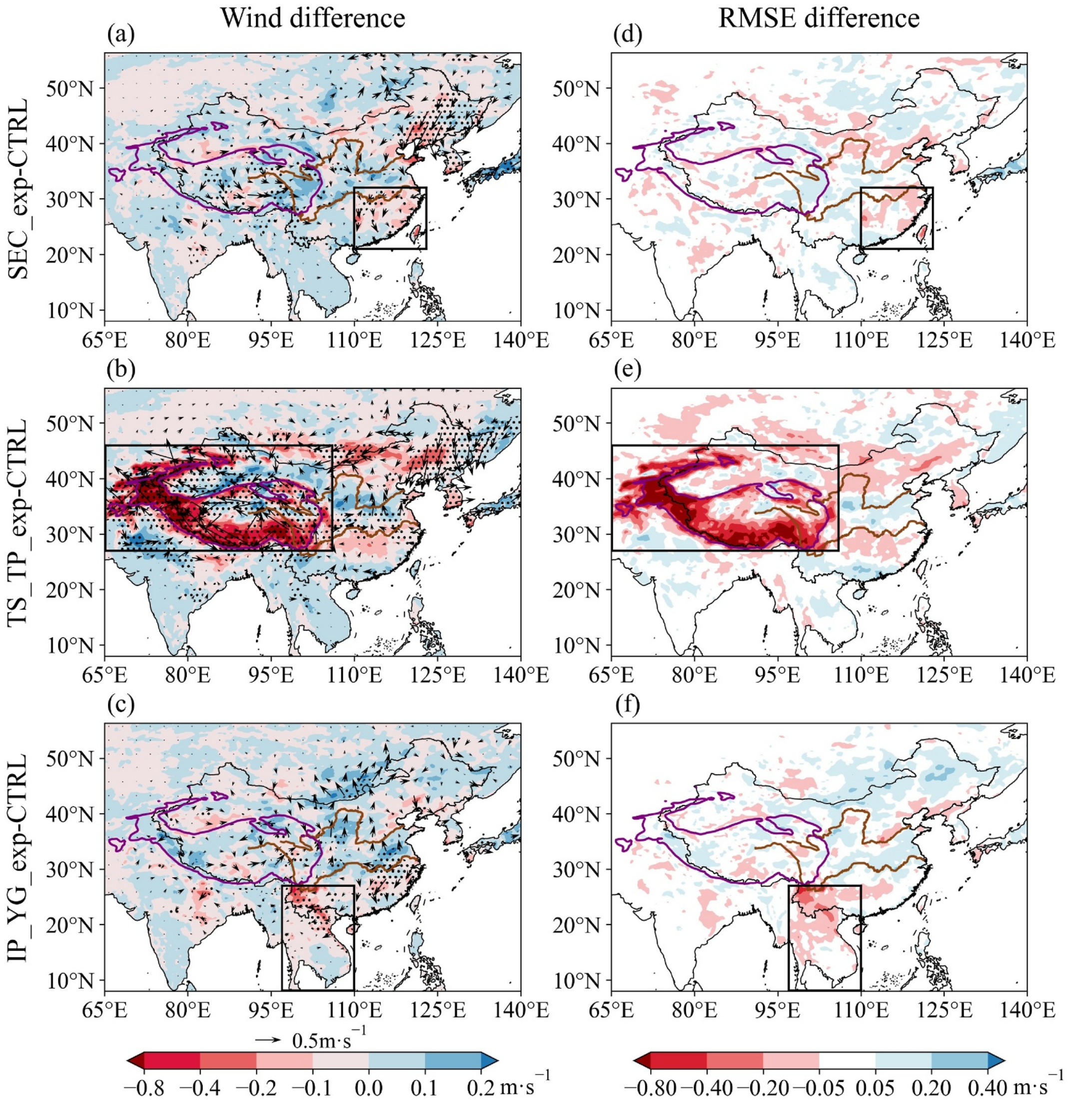

Figure 5. The differences of the simulated wind vector and speed (color shadings) at 10 m above the ground between each sensitivity experiment and the CTRL experiment (a–c); and the differences in the RMSE of the simulated wind speed at 10 m above the ground between each sensitivity experiment and the CTRL experiment (d–f). The black rectangles show the regions where the sub-grid turbulent orographic form drag scheme is activated in each sensitivity experiment. The purple contour lines represent the elevation of 3,000 m. The brown lines depict the Yangtze River and Yellow River. The differences that pass the 90% significance level are dotted.

Mountains and TP, such as 925 hPa and 850 hPa, most areas are obstructed by terrain barriers, resulting in smaller magnitudes and disordered directions of the STOFD (Figures 4a and 4b, rectangle C). At 700 hPa, the direction of STOFD on the north side adjacent to the TP is toward the east (Figure 4c, rectangle C). Conversely, near the Tianshan Mountains, the STOFD direction is westward. The STOFD of the Indochina Peninsula and Yunnan-Guizhou Plateau is particularly noteworthy at 925 hPa and 850 hPa, primarily situated in the northern region of the Indochina Peninsula and the southern part of the Yunnan-Guizhou Plateau (Figures 4a and 4b, rectangle D). The prevailing direction of the STOFD in this area is westward.

The influence of the STOFD on the 10 m wind simulation corresponds well with the STOFD in each sensitivity experiment and is the most significant in the sub-region where the STOFD is enabled (Figures 5a–5c). In the TS_TP_exp experiment, the STOFD significantly weakens the 10 m wind speed over the Tianshan Mountains and TP (Figure 5b), resulting in a notably reduced RMSE of simulated wind at 10 m in these regions compared to the CTRL experiment (Figure 5e). Although not as significant as those in the TS_TP_exp experiment, the remote effects of the STOFD in the IP_YG_exp experiment lead to a notable reduction of the simulated 10 m wind speed and its RMSE over the Indochina Peninsula and Yunnan-Guizhou Plateau compared with the CTRL experiment (Figures 5c and 5f). Among the 3 sensitivity experiments, the local effects of the STOFD in the SEC_exp lead to the most significant reduction of the simulated 10 m wind speed and its RMSE in the Southeastern China compared with the CTRL experiment (Figures 5a and 5d). It's worth noting that ERA5, which also uses the STOFD scheme, does not use observations of 10 m winds over land, but instead follows model profiles driven by the analysis of upper air data. Therefore, a portion of the reduction in RMSE can be attributed to the inclusion of the STOFD scheme in ERA5 for calculating 10 m wind, this confirms the accurate application of the STOFD scheme in RegCM4.

Even though the effects of the STOFD within the Tianshan Mountains and TP show the most significant improvement of the 10 m wind speed simulation in the region with the most complex sub-grid terrain in the model domain, the same cannot be said for its impact on precipitation simulation in Eastern China. However, there is still evidence to suggest that the STOFD exhibits favorable capabilities for enhancing the precipitation simulation performance in Eastern China. The relationship between the improvements of 10 m wind speed simulations and those of precipitation simulations is complex and nonlinear, with even minor alterations in wind patterns leading to obvious changes in precipitation compared to the CTRL experiment.

Combined with Figures 4 and 5 illustrates a direct impact of the STOFD on the 10 m wind, showcasing a strong correlation between the changes in wind direction and speed with the STOFD. By decomposing the impact of 10 m wind into various levels corresponding to the STOFD in Figure 7, the underlying formation mechanism of atmospheric circulation field disparities is uncovered.

Previous studies have shown that the development of wind is highly influenced by the background circulation (Chang, 2014; Ching et al., 2010; B. Li et al., 2022; Pepler et al., 2018), so do the wind differences between each sensitivity experiment and the CTRL experiment. The atmospheric circulation fields at different levels in the CTRL experiment are shown in Figure 6 as the background circulation for the development of wind difference between each sensitivity experiment and the CTRL experiment.

From Figures 6a–6d, at 600 hPa and below, there is a deep monsoon trough near the Southeastern China around 20°N. Additionally, a monsoon trough can be seen between the Bay of Bengal (labeled in Figure 1a) and the Indochina Peninsula, which is a distinguishing feature of the South Asian summer monsoon (Choudhury & Krishnan, 2011; Krishnamurti & Surgi, 1987). A weak ridge separates these two troughs. The east part of the trough acts as a dynamic trough, characterized by strong convergence and moisture accumulation, creating a favorable dynamic condition for the development of cyclone (Choudhury & Krishnan, 2011; Das, 1986; Sikka & Narasimha, 1995). A high-pressure ridge is present in the low-level troposphere over the Northern China and moves southwest in the mid-level. In the Northeastern China, a transversal trough forms at the low-level troposphere, which is then replaced by a westerly trough at the mid-level troposphere. At higher levels, the Northern China is located between the westerly trough and high-pressure ridge, with prevailing northwest winds, which is conducive to the development of downward motion. A westerly ridge appears on the northwest side of China at the middle and upper levels. Due to the thermal difference between TP and its surrounding terrains in summer, a cyclone appears over TP. The low-pressure center gives rise to a trough, while a ridge forms on the east side of the trough. On the northwest side of TP, a high-pressure ridge appears due to the lower temperature in the Tarim Basin (labeled in Figure 1a) compared to the surroundings.

Compared to the CTRL experiment, the SEC_exp experiment produces a significant decrease of the local wind speed in the low-level troposphere corresponding to the STOFD, which diminishes as altitude increases in the mid-upper troposphere (Figures 7a–7f). This deceleration of wind is directly generated by the southward STOFD, resulting in an increase in wind speed on both sides of the deceleration. The wind shear caused by the difference between north and south winds on each side of the deceleration leads to anticyclonic and cyclonic disturbances on the west and east sides of the deceleration, respectively. The cyclonic disturbance on the east side is induced and promoted by the monsoon trough, forming a cyclone difference between the SEC_exp experiment and the CTRL experiment. While the anticyclonic disturbance on the west side is suppressed by the westerly winds and does not exhibit further development. Along with the direction of background circulation, the cyclone difference between the SEC_exp experiment and the CTRL experiment propagates northward. This cyclonic difference deepens and expands in the lower and middle levels in the northeast side of China due to the influence of the transversal trough and monsoon trough in the Northeastern China, respectively.

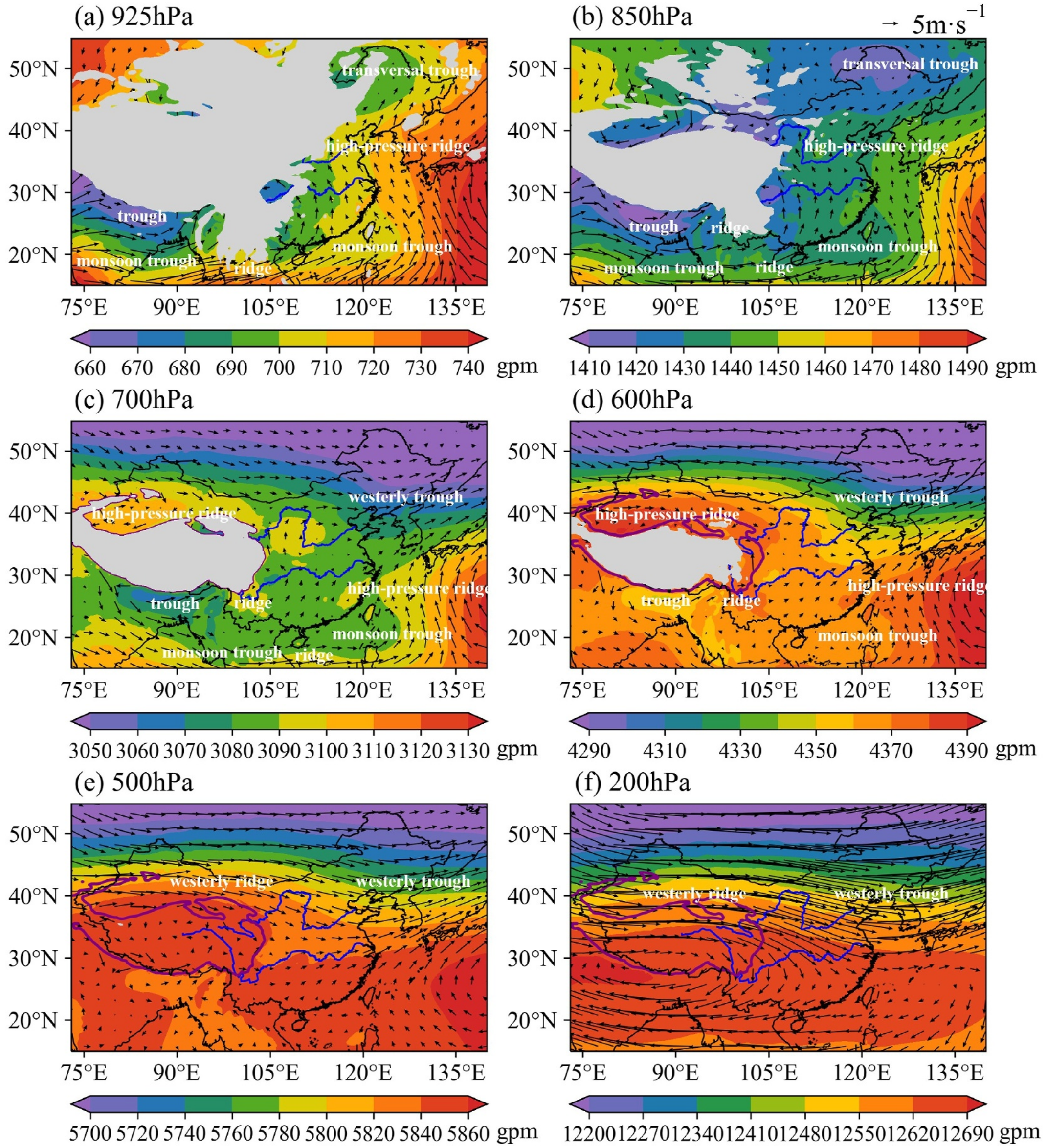

Figure 6. The wind vector and geopotential height (color shadings) in the CTRL experiment at different levels. The significant troughs and ridges associated with the development of circulation differences are labeled by white text. The gray shadow indicates the terrain height is higher than the altitude of the air pressure level. The purple contour lines represent the elevation of 3,000 m. The blue lines depict the Yangtze River and Yellow River.

As shown in Figures 7g–7l, the STOFD of Tianshan Mountains and TP greatly weakens the westerly winds on the north side of TP in the mid-level troposphere, creating a pronounced easterly difference compared to situations in the CTRL experiment. On both sides of the easterly difference, the flow is accelerated. The winds at the levels with relatively weaker STOFD are primarily influenced by the remote effects of the substantial STOFD at other levels. The contrasting easterly and westerly wind differences between the TS_TP_exp experiment and the CTRL experiment produce the wind shear differences, which generate cyclonic and anti-cyclonic disturbances on the south and north sides of the easterly difference, respectively. The presence of a high-pressure ridge in the Tarim Basin and a trough on the southern side of TP contribute to the development of these disturbances (Figures 6c and 6d), further resulting in the formation of corresponding anticyclonic and cyclonic differences between the TS_TP_exp experiment and the CTRL experiment. The deceleration and acceleration compared to the CTRL experiment produced by the STOFD of Tianshan Mountains and TP spread southwest along the direction of the mid-level wind, leading to easterly differences in the middle and lower

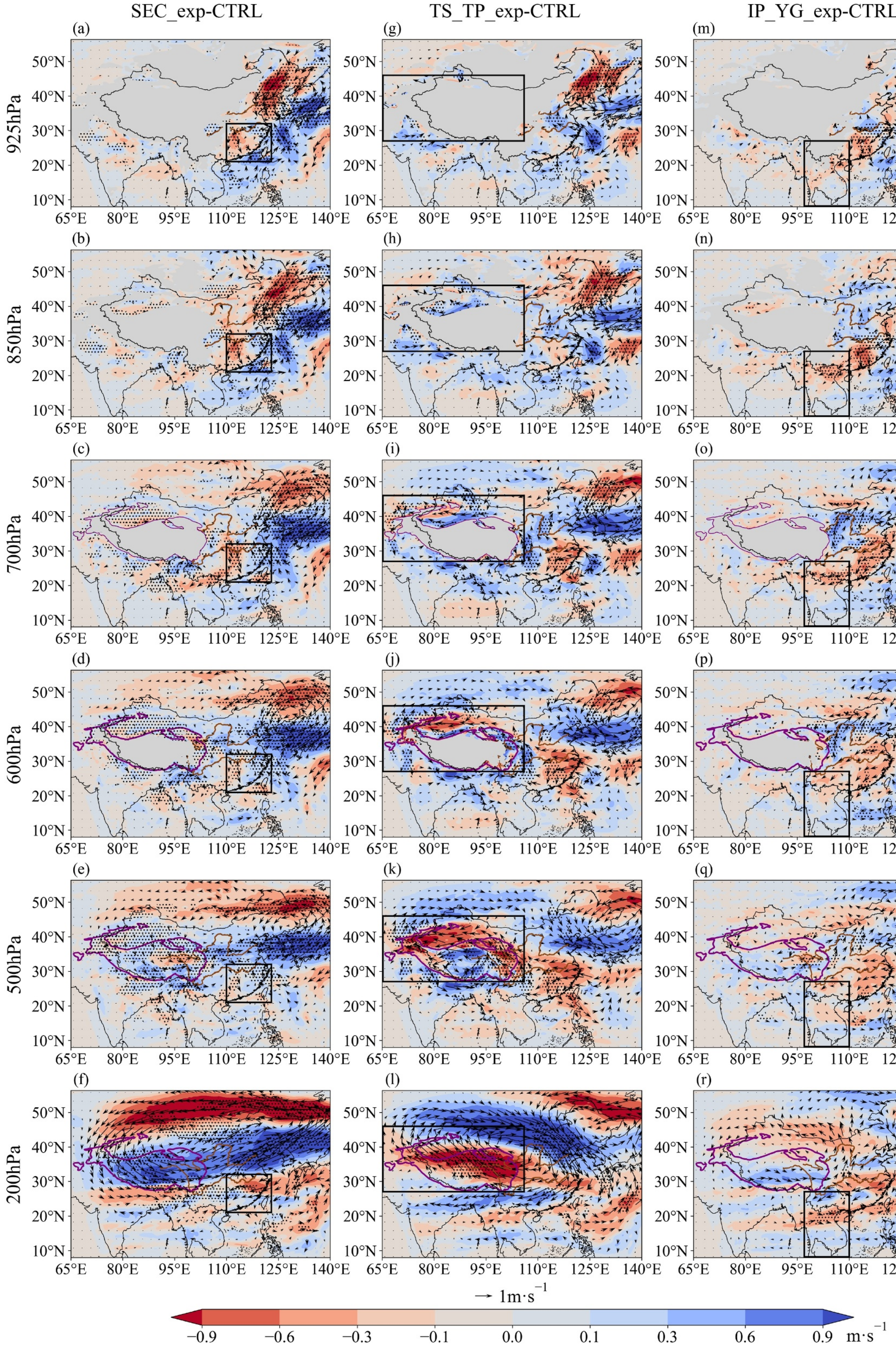

Figure 7. Distribution of wind vector and speed (color shadings) differences at different levels; from left to right are the differences between each of the SEC_exp, TS_TP_exp and IP_YG_exp experiment and the CTRL experiment. The black rectangles indicate the regions with the sub-grid turbulent orographic form drag scheme activated in each sensitivity experiment. The gray shadow indicates the terrain height is higher than the altitude of the air pressure level. The purple contour lines represent the elevation of 3,000 m. The brown lines depict the Yangtze River and Yellow River. The differences that pass the 90% significance level are dotted.

reaches of the Yangtze River and westerly differences on either side of the easterly differences. The interaction between the shear differences and the background monsoon trough leads to the formation of a new cyclone difference compared with the situation of the CTRL experiment. In addition, an updraft prevails in the background trough in the northeast side of China. The updraft is intensified by the westerly difference and forms a cyclone difference in the northeast side of China between the TS_TP_exp experiment and the CTRL experiment. Meanwhile, the anticyclonic difference compared to the situation in the CTRL experiment on the northern side of TP moves downstream, creating a fresh center of high-pressure difference between these two cyclonic differences. The high-pressure difference is further strengthened by the influence of downdraft in the front ridge to the back of the trough. This high-pressure difference weakens slightly at lower levels and eventually merges with the anticyclonic difference on the northern side of TP in the upper troposphere under the influence of the westerly ridge.

The STOFD of the Indochina Peninsula and Yunnan-Guizhou Plateau causes a slowdown in the westerly in the north of the Indochina Peninsula and the south of the Yunnan-Guizhou Plateau, while accelerating them on both sides of the deceleration zone (Figures 7m–7r). Compared to the CTRL experiment, the wind shear differences in the south side of the deceleration meet the South Asian monsoon trough at the mid-level troposphere, forming a cyclonic difference and developing downstream. The cyclonic difference then deepens into a center of low-pressure difference at another monsoon trough. The wind shear variations on the north side of the deceleration meet the ridge on the south side of TP to generate an anticyclone difference between the IP_YG_exp experiment and the CTRL experiment. The anticyclonic difference deepens over the Northern China because of meeting lower reaches of the ridge in the Northern China.

Comparing the circulation differences between each sensitivity experiment and the CTRL experiment, the intensity of cyclonic difference in the Southeastern China induced by the local effects of the STOFD is weaker than those generated by the remote effects of the STOFD due to relatively smaller magnitude of STOFD over the Southeastern China. While in the Southeastern China, where the local effects of the STOFD have a major impact, the cyclone differences induced by the local effects of the STOFD are more localized.

These cyclonic and anticyclonic differences between each sensitivity experiment and the CTRL experiment stimulate the vertical motion changes, so the dynamic foundation is laid for the improvement of precipitation simulation. However, the magnitude of changes in vertical velocity is not exactly consistent with the circulation differences due to the influence of other factors.

Due to the differences in the wind field between each sensitivity experiment and the CTRL experiment, there are changes in the water vapor flux convergence as shown in Figure 8. The eastern part of China, which is located near the coast, has abundant water vapor. Although there are atmospheric circulation differences over the Western China between each sensitivity experiment and the CTRL experiment, the most significant disparities in water vapor flux convergence are located in Eastern China. This could potentially explain why the improvement of simulated precipitation primarily appears in Eastern China. The local cyclonic difference between the SEC_exp experiment and the CTRL experiment in the Southeastern China results in the convergence of airflow, thereby increasing the convergence of water vapor flux in the Southeastern China (Figure 8b). In the TS_TP_exp experiment, the corresponding cyclonic (anticyclonic) difference between the TS_TP_exp experiment and the CTRL experiment in the Southeastern China (Northern China) promotes the increase (decrease) in convergence of water vapor flux (Figure 8c). The changes of water vapor flux convergence generated by the STOFD effects of the Indochina Peninsula and Yunnan-Guizhou Plateau are roughly the same as those generated by effects of the STOFD over the Tianshan Mountains and TP (Figure 8d). Even though there are cyclonic (anticyclonic) differences and water vapor convergence differences compared to the CTRL experiment over the Southeastern China (Northern China) in the SEC_exp, TS_TP_exp, and IP_YG_exp (TS_TP_exp and IP_YG_exp) experiments, discrepancies still exist among the different sensitivity experiments. Compared to the CTRL experiment, the SEC_exp experiment produced cyclonic and water vapor flux convergence differences covering the entire Southeastern China. Whereas those differences are partly located in the Southeastern China in the TS_TP_exp and IP_YG_exp experiments. Furthermore, in the IP_YG_exp experiment, there also exists a decrease in water vapor flux convergence over the west part of Southeastern China compared to the CTRL experiment (Figure 8d), hindering precipitation production over these regions. However, the increased convergence of water vapor flux and the cyclonic differences in the other parts of the Southeastern China in the IP_YG_exp experiment both contribute to the increase of precipitation there. The increase in water vapor induced by the local effects of the

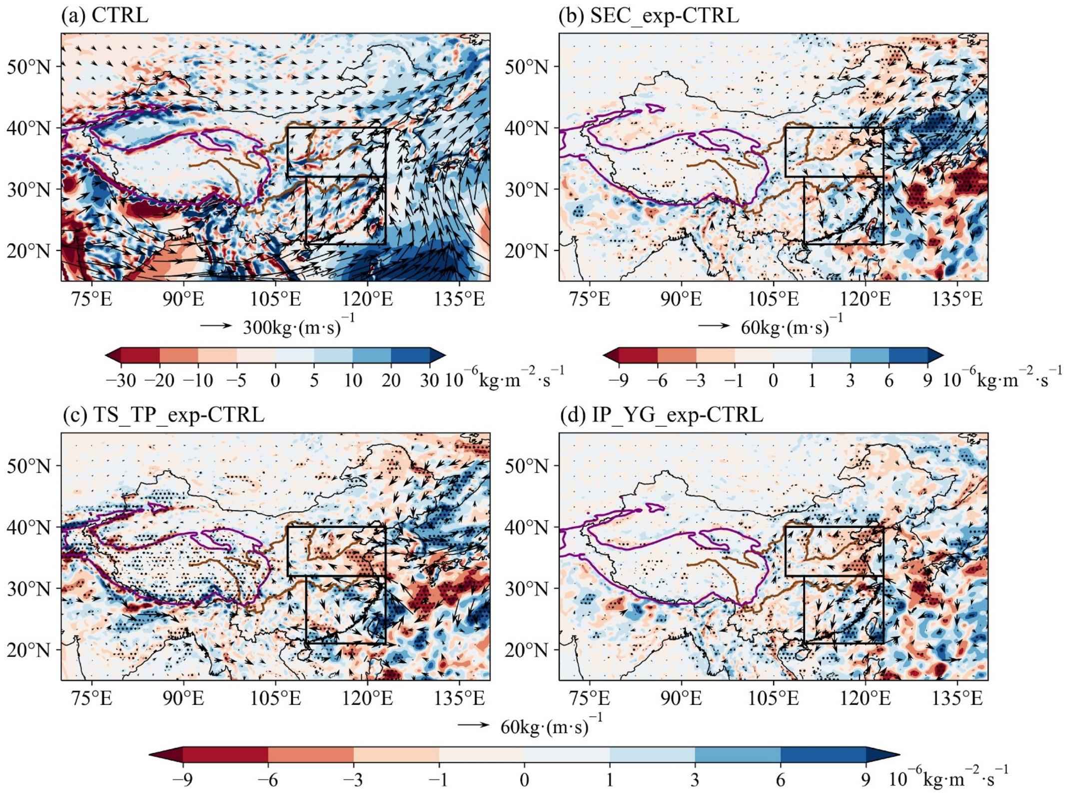

Figure 8. Spatial distribution of water vapor flux (vector) integrated from surface to 300 hPa and its convergence (color shadings) in the CTRL experiment (a), and their differences between each sensitivity experiment and CTRL experiment (b–d). The black rectangles indicate the Southeastern China and Northern China as shown in Figure 2a. The purple contour lines represent the elevation of 3,000 m. The brown lines depict the Yangtze River and Yellow River. The differences that pass the 90% significance level are dotted.

STOFD mainly occurs in the Southeastern China, with the remote effects of the STOFD only increasing the water vapor flux convergence in part of this region. In the Northern China, the remote effects of the STOFD in both the IP_YG_exp and the TS_TP_exp experiment produce remarkable decreased water vapor flux convergence compared to the CTRL experiment.

The convective available potential energy (CAPE) increases in the Southeastern China while decreases in the Northern China in the sensitivity experiments (Figure 9). Except for TS_TP_exp, the differences of CAPE correspond well with the differences of water vapor flux convergence mentioned above. It suggests that the differences in CAPE are notably influenced by changes in regional water vapor content caused by the differences of water vapor flux convergence. Apart from the water vapor flux convergence, many other factors may also impact the CAPE, but no significant corresponding has been demonstrated thus far. Although the decrease of water vapor flux convergence over the Northern China is more obvious in the TS_TP_exp experiment than in the SEC_exp experiment (Figures 8b and 8c), the change of CAPE remains relatively unaffected (Figures 9b and 9c). This could be attributed to the influence of other factors such as the thermodynamic environment (not shown). The local effects of the STOFD significantly boost the CAPE in most areas of the Southeastern China (Figure 9b), whereas the remote effects of the STOFD are relatively minimal or affect only a small part of the region compared to the impact of local effects (Figures 9c and 9d).

The differences in CAPE facilitate vertical motion differences in Eastern China (Figure 10). Notably, compared to the CTRL experiment, the significant increases of CAPE in the Southeastern China produced by the SEC_exp experiment facilitate the occurrence of updrafts (Figure 10b). In the IP_YG_exp experiment, the CAPE only increases in a small part of the Southeastern China, and even decreases in the rest region compared to the CTRL experiment, hindering the occurrence of updrafts (Figure 10d). Relative to the CTRL experiment, the significantly reduced CAPE in the IP_YG_exp experiment over the Northern China greatly inhibits updrafts.

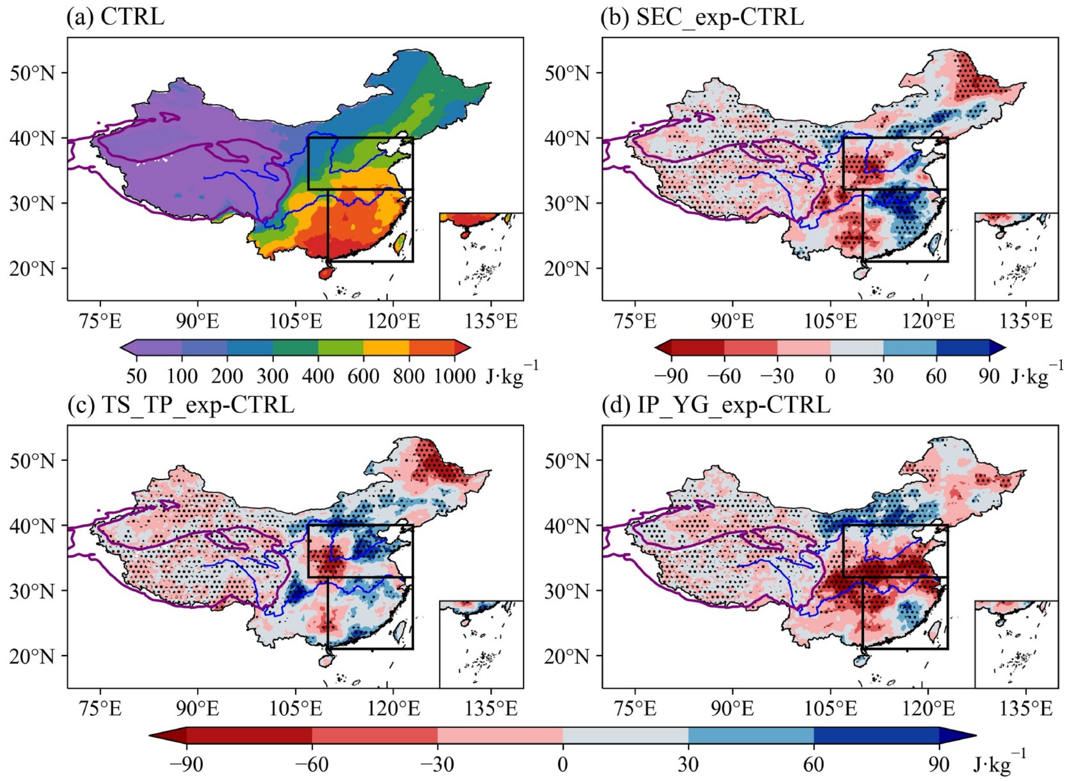

Figure 9. Spatial distribution of convective available potential energy in the CTRL experiment (a), and its differences between each sensitivity experiment and the CTRL experiment (b–d). The dark rectangles indicate the Southeastern China and Northern China as shown in Figure 2a. The purple contour lines represent the elevation of 3,000 m. The blue lines depict the Yangtze River and Yellow River. The differences that pass the 90% significance level are dotted.

Previous research of Van Den Dool (1987) demonstrated a strong correlation between vertical motion at 500 hPa and precipitation. Consequently, Figures 10a–10d further show the vertical velocity at 500 hPa in the CTRL experiment, along with the differences of vertical velocity at 500 hPa between each sensitivity experiment and the CTRL experiment. It is clearly noted that the vertical motion differences exhibit strong correspondence with precipitation differences in all the sensitivity experiments. To explore the source of this strong correspondence, the lead-lag correlation coefficients between 500 hPa vertical velocity differences and precipitation differences produced by each sensitivity experiment relative to the CTRL experiment have been calculated. Due to the consistent results across all sensitivity experiments, only the correlation coefficient between the 500 hPa vertical velocity differences and precipitation differences produced by the SEC_exp relative to the CTRL experiment is presented (Figures 10e–10h). The 500 hPa vertical velocity differences at 3 hr ahead the precipitation show the largest relations with the precipitation differences, suggesting that the 500 hPa vertical velocity differences contribute to the precipitation differences and the precipitation corresponds well with the vertical velocity.

The vertical velocity differences at 500 hPa level between each sensitivity experiment and the CTRL experiment can be primarily attributed to the upward and downward motion differences resulting from cyclonic and anticyclonic differences. Furthermore, the CAPE differences between each sensitivity experiment and the CTRL experiment can either inhibit or promote the development of vertical motion.

Including the STOFD of the microscale orography can improve the climate simulation by blocking partial airflow, which highly resembles the effect of mesoscale orography. Compared to the sub-grid mesoscale terrain-generated orographic gravity wave drag in previous studies, the STOFD exhibited in this research is of a much smaller magnitude (Van Niekerk et al., 2018). As a result, the blocking effect of STOFD on airflow is also less pronounced than that of the gravity wave drag (Liu et al., 2023; Van Niekerk et al., 2018). This finding is consistent with previous research (Zhou, Beljaars, et al., 2017). Furthermore, the orographic gravity wave drag typically

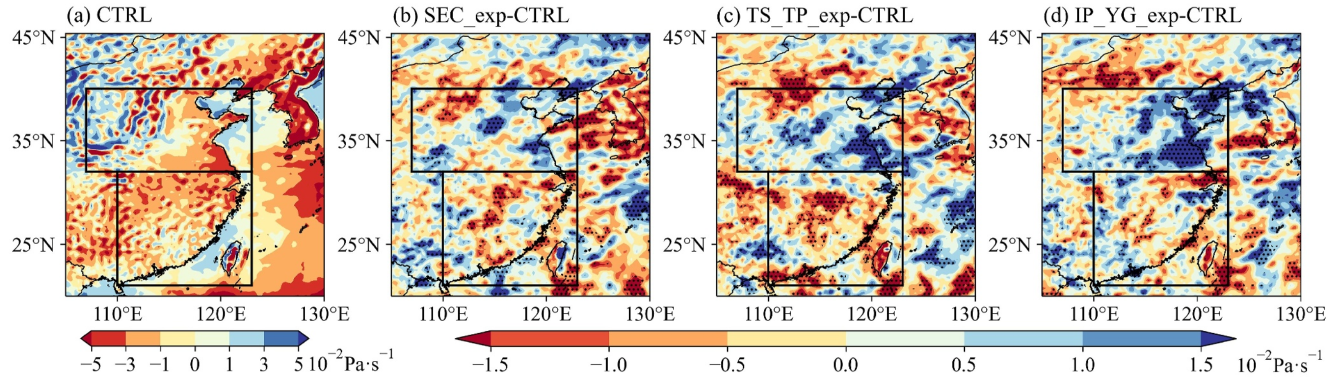

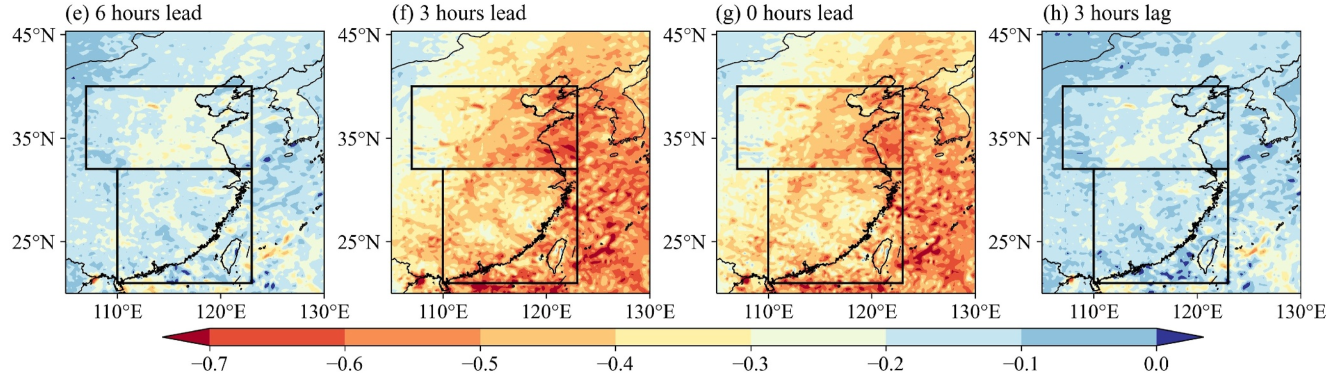

Figure 10. The vertical velocity at 500 hPa level over Eastern China in the CTRL experiment (a), and its difference between each sensitivity experiment and the CTRL experiment (b–d). The lead-lag correlation coefficient between 500 hPa vertical velocity differences and precipitation differences in the SEC_exp experiment relative to the CTRL experiment is represented in panels (e–f). The lead (lag) of n hours means the 500 hPa vertical velocity differences leading (lagging) the precipitation differences by n hours. The black rectangles indicate the Southeastern China and Northern China as shown in Figure 2a. The differences passing the 90% significance level are dotted.

occurs in the lower and upper levels due to the break of upward-propagating orographic gravity waves, while the STOFD is more obviously produced near the surface (Kim et al., 2003; Zhang et al., 2020). Despite its relatively modest magnitude and impact in comparison to the mesoscale orography, this study highlights the clear climatic effects of micro-scale orography that should not be overlooked.

Overall, both the local and remote effects of the STOFD significantly affect the formation of wind differences between each sensitivity experiment and the CTRL experiment, leading to discrepancies in cyclone and anti-cyclone when interacting with troughs and ridges. Subsequently, these disparities result in fluctuations of water vapor flux convergence in Eastern China where abundant water vapor is present. Cyclonic (anticyclonic) differences generate upward (downward) vertical velocity differences, which are facilitated by increased (decreased) CAPE. The combined effects of these cyclonic (anticyclonic) differences, along with the differences in the water vapor flux convergence, CAPE and vertical motion, contribute to the simulated precipitation differences in each sensitivity experiment compared to the CTRL experiment. In the Southeastern China, the local effects of the STOFD produce a cyclonic difference that is locally concentrated and delivers water vapor over a large area of the Southeastern China. Also, the CAPE is greatly increased and the upward movement is intensified. While the cyclonic differences generated by the remote effects of the STOFD within the Indochina Peninsula and Yunnan-Guizhou Plateau, and the Tianshan Mountains and TP are more intense, they only generate relatively little water vapor flux convergence in the Southeastern China compared to that induced by the local effects. And the increases of CAPE are weaker than those generated by the local effects of the STOFD. Therefore, the local effects of the STOFD correct the underestimation of precipitation in the Southeastern China more significantly compared to the remote effects. The remote effects of the STOFD within the Indochina Peninsula and Yunnan-Guizhou Plateau, as well as the Tianshan Mountains and TP, greatly improve the accuracy of summer precipitation simulation in Eastern China due to their notable disturbances.

5. Conclusions

Inclusion of the STOFD in the RegCM4 can remarkably improve the summer monsoon precipitation simulation in Eastern China, while the remote effects of the STOFD have not yet been revealed quantitatively. This study conducts a series of sensitivity experiments using the RegCM4 adopting the STOFD scheme to examine the impact of local and remote effects of the STOFD on precipitation simulation.

The results indicate that the local effects of the STOFD within the Southeastern China with complex sub-grid terrains has the most significant impact on the improvement of the summer precipitation simulation in this region. The local effects of the STOFD within the Southeastern China results in the absolute error and the RMSE of the precipitation simulation in this region reduced by 37.1% and 10.7%, respectively. Conversely, the improvement of the precipitation simulation in the Northern China with mild sub-grid topography is primarily induced by the remote effects of the STOFD. Specifically, the STOFD of the Indochina Peninsula and Yunnan-Guizhou Plateau has the most pronounced impact, contributing to the absolute error and the RMSE of the precipitation simulation in this region reduced by 90.1% and 32.9%, respectively.

In addition, the process of the local and remote effects of the STOFD affecting precipitation is also revealed. The STOFD generates wind differences opposite to the background wind direction. Promoted by the background circulation, these wind differences form cyclonic and anticyclonic differences between each sensitivity experiment and the CTRL experiment. The circulation disturbances induced by the remote effects of the STOFD propagate downstream to Eastern China. Both cyclonic and anticyclonic differences generated by the local and remote effects of the STOFD produce corresponding water vapor flux convergence differences. The differences of CAPE in sensitivity experiments relative to the CTRL experiment further influence the development of vertical motion associated with cyclonic and anticyclonic differences. All these differences of meteorological factors ultimately contribute to the improvement of precipitation simulation. The influence of the local effects of the STOFD on the precipitation simulation in the Southeastern China is more pronounced compared to those induced by the remote effects of the STOFD. This is due to the cyclonic differences, corresponding water vapor flux convergence differences, CAPE variations and vertical velocity differences induced by the local effects of the STOFD are more concentrated in this region. The relatively larger magnitudes of the remote effects of the STOFD within both the Tianshan Mountains and TP, Indochina Peninsula and Yunnan-Guizhou Plateau and their resulting disturbances play a significant role in the improvement of summer precipitation simulation in the Northern China with mild sub-grid terrain. The impact of the STOFD within the Indochina Peninsula and Yunnan-Guizhou Plateau on the precipitation simulation is particularly pronounced in the Northern China, resulting in the most significant enhancement of precipitation simulation performance. Although not the largest, the remote effects of the STOFD within the Tianshan Mountains and TP play the second significant role in improving the summer precipitation simulation in both the Southeastern and Northern China.

This study recognizes the remote impact of STOFD of Tianshan Mountains and TP in improving the summer precipitation simulation in Eastern China, which is consistent with previous studies (Chiang et al., 2020; Kong & Chiang, 2020; Son et al., 2020). Different from the deduction of Gu et al. (2023b), this study discovers that the vertical velocity differences in the mid-level troposphere exhibit strong correspondence with precipitation differences in all the sensitivity experiments. Therefore, this strong relationship is not solely attributed to the STOFD of Tianshan Mountains and TP. This study also emphasizes the remote effects of the STOFD within the Indochina Peninsula and Yunnan-Guizhou Plateau on the summer precipitation simulation in the Northern China and the local effects of the STOFD within the Southeastern China on the summer precipitation simulation in this region.

Nevertheless, there are still several deficiencies in this study that require further improvement. Although the STOFD scheme applied in this study is widely recognized and utilized in various numerical models, it still has its constraints. This scheme is based on the surface stress and vertical distribution derived from two-dimensional sinusoidal hills, rather than accounting for the complexities of actual sub-grid orography (Beljaars et al., 2004; Wood et al., 2001; Xue & Shen, 2023). Furthermore, the STOFD calculated by this scheme is not sensitive to boundary-layer stability (Beljaars et al., 2004). Thus, there is a pressing need for further research to refine the STOFD scheme to obtain more accurate simulations and predictions. Recently, Xue and Shen (2023) proposed a STOFD scheme that considers three-dimensional hills and incorporates the angle direction of low-level wind and terrain, remedying the limitations of the previous two-dimensional approach. This scheme will be applied in future studies to further enhance the model's ability to represent micro-scale terrain. In addition, the conclusions obtained by this study may rely on the regional model used. The sub-grid terrain data with ~1 km resolution used in this study may be too coarse to some extent. Besides, the focus on only two regions representing the areas with mild and complex sub-grid terrain may limit the generalization of the conclusions. It is recommended that more regions representing various sub-grid terrains are included and use much finer sub-grid terrain data in future studies to provide a more comprehensive analysis.

Data Availability Statement

Data-The data used in this study include the 0.25° × 0.25° gridded precipitation daily products provided by the Asian Precipitation - Highly Resolved Observational Data Integration Towards Evaluation (APHRODITE, 2012), the fifth generation ECMWF atmospheric reanalysis of the global climate (ERA5) with a horizontal resolution of 0.25° × 0.25° (ECMWF, 2020) and the replay of the land component of the ERA5 reanalysis with a finer spatial resolution of 0.1° × 0.1° (ECMWF, 2019). Additionally, the 1° × 1° NOAA Optimum Interpolation Sea Surface Temperature (OISST, NOAA, 2002) and the 1.5° × 1.5° ERA-Interim Reanalysis (ECMWF, 2011), along with the 0.25° × 0.25° European Space Agency (ESA) Climate Change Initiative (CCI) Essential Climate Variable (ECV) Surface Soil Moisture and Combined Product (Dorigo et al., 2021) are used for numerical simulations. Grid-scale Topography is derived from 30″ × 30″(~1 km) Global Multi-resolution Terrain Elevation Data (GMTED, Danielson & Gesch, 2011) developed by the U.S. Geological Survey (USGS). Software-To carry out the simulations, the REGCM4 (ICTP, 2016) and RegCM4 with a STOFD scheme (Gu et al., 2023a) are utilized.

Acknowledgments
This study is supported by the National Natural Science Foundation of China under Grant 42375157, the National Key R&D Program of China under Grant 2022YFC3080500, the Beijige Open Research Fund under Grant BJG202403, the CAS "Light of West China" Program (E129030101), Open Research Fund Program of Plateau Atmosphere and Environment Key Laboratory of Sichuan Province (PAEKL-2023-K01), the Research Funds for the Frontiers Science Center for Critical Earth Material Cycling Nanjing University, the Fundamental Research Funds for the Central Universities (020914380103), the Jiangsu University "Blue Project" outstanding young teachers training object, and the Jiangsu Collaborative Innovation Center for Climate Change. We appreciate the High Performance Computing Center of Nanjing University, and the National Key Scientific and Technological Infrastructure project "Earth System Numerical Simulation Facility" (EarthLab) for providing us with computing resources. We are grateful to APHRODITE, ECWMF, NOAA, USGS, and ESA for providing data. We appreciate ICTP for providing the source codes of RegCM4 (https://github.com/ictp-esp/RegCM). We sincerely appreciate all the reviewers' valuable insights and detailed feedback in improving our manuscript.

References

APHRODITE. (2012). A long-term daily gridded precipitation dataset for Asia based on a dense network of rain gauges [Datasets]. *APHRODITE*. Retrieved from http://aphrodite.st.hirosaki-u.ac.jp/download/

Ashfaq, M., Cavazos, T., Reboita, M. S., Torres-Alavez, J. A., Im, E.-S., Olusegun, C. F., et al. (2021). Robust late twenty-first century shift in the regional monsoons in RegCM-CORDEX simulations. *Climate Dynamics*, *57*(5–6), 1463–1488. https://doi.org/10.1007/s00382-020-05306-2

Babaei, M., Alizadeh, O., & Irannejad, P. (2021). Impacts of orography on large-scale atmospheric circulation: Application of a regional climate model. *Climate Dynamics*, *57*(7–8), 1973–1992. https://doi.org/10.1007/s00382-021-05790-0

Baldwin, J., & Vecchi, G. (2016). Influence of the Tian Shan on arid extratropical Asia. *Journal of Climate*, *29*(16), 5741–5762. https://doi.org/10.1175/JCLI-D-15-0490.1

Belcher, S. E., & Wood, N. (1996). Form and wave drag due to stably stratified turbulent flow over low ridges. *Quarterly Journal of the Royal Meteorological Society*, *122*(532), 863–902. https://doi.org/10.1002/qj.49712253205

Beljaars, A. C. M., Brown, A. R., & Wood, N. (2004). A new parametrization of turbulent orographic form drag. *Quarterly Journal of the Royal Meteorological Society*, *130*(599), 1327–1347. https://doi.org/10.1256/qj.03.73

Berg, P., Wagner, S., Kunstmann, H., & Schädler, G. (2013). High resolution regional climate model simulations for Germany: Part I—Validation. *Climate Dynamics*, *40*(1), 401–414. https://doi.org/10.1007/s00382-012-1508-8

Blumen, W. (1988). The effects of a periodic upstream flow on nonlinear hydrostatic mountain waves. *Journal of the Atmospheric Sciences*, *45*(22), 3460–3469. https://doi.org/10.1175/1520-0469(1988)045<3460:TEOAPU>2.0.CO;2

Chang, E. K. M. (2014). Impacts of background field removal on CMIP5 projected changes in Pacific winter cyclone activity. *Journal of Geophysical Research: Atmospheres*, *119*(8), 4626–4639. https://doi.org/10.1002/2013jd020746

Chen, J., & Bordoni, S. (2014). Orographic effects of the Tibetan Plateau on the East Asian summer monsoon: An energetic perspective. *Journal of Climate*, *27*(8), 3052–3072. https://doi.org/10.1175/JCLI-D-13-00479.1

Chen, L., Gu, W., & Li, W. (2019). Why is the east Asian summer monsoon extremely strong in 2018? Collaborative effects of SST and snow cover anomalies. *Journal of Meteorological Research*, *33*(4), 593–608. https://doi.org/10.1007/s13351-019-8200-4

Chiang, J. C. H., Kong, W., Wu, C. H., & Battisti, D. S. (2020). Origins of East Asian summer monsoon seasonality. *Journal of Climate*, *33*(18), 7945–7965. https://doi.org/10.1175/jcli-d-19-0888.1

Ching, L., Sui, C. H., & Yang, M. J. (2010). An analysis of the multiscale nature of tropical cyclone activities in June 2004: Climate background. *Journal of Geophysical Research*, *115*(D24), D24108. https://doi.org/10.1029/2010jd013803

Choudhury, A. D., & Krishnan, R. (2011). Dynamical response of the South Asian monsoon trough to latent heating from stratiform and convective precipitation. *Journal of the Atmospheric Sciences*, *68*(6), 1347–1363. https://doi.org/10.1175/2011JAS3705.1

Danielson, J. J., & Gesch, D. B. (2011). Global multi-resolution terrain elevation data 2010 (GMTED2010) [Datasets]. *USGS*. https://doi.org/10.3133/ofr20111073

Das, P. K. (1986). Monsoons, WMO Rep. *613*, 115 pp.

Dee, D. P., Uppala, S. M., Simmons, A. J., Berrisford, P., Poli, P., Kobayashi, S., et al. (2011). The ERA-interim reanalysis: Configuration and performance of the data assimilation system. *Quarterly Journal of the Royal Meteorological Society*, *137*(656), 553–597. https://doi.org/10.1002/qj.828

Ding, Y. (1992). Summer monsoon rainfalls in China. *Journal of the Meteorological Society of Japan. Ser. II*, *70*(1B), 373–396. https://doi.org/10.2151/jmsj1965.70.1B_373

Ding, Y., & Chan, J. (2005). The East Asian summer monsoon: An overview. *Meteorology and Atmospheric Physics*, *89*(1–4), 117–142. https://doi.org/10.1007/s00703-005-0125-z

Dorigo, W., Preimesberger, W., Moesinger, L., Pasik, A., Scanlon, T., Hahn, S., et al. (2021). ESA soil moisture climate change initiative (Soil_Moisture_cci): COMBINED product. Version 06.1 [Dataset]. *NERC EDS Centre for Environmental Data Analysis*. Retrieved from https://catalogue.ceda.ac.uk/uuid/43d73291472444e6b9c2d2420dbad7d6

Duan, A., Hu, D., Hu, W., & Zhang, P. (2020). Precursor effect of the Tibetan plateau heating anomaly on the seasonal March of the East Asian summer monsoon precipitation. *Journal of Geophysical Research: Atmospheres*, *125*(23), e2020JD032948. https://doi.org/10.1029/2020jd032948

Duan, A., Wu, G., Liu, Y., Ma, Y., & Zhao, P. (2012). Weather and climate effects of the Tibetan Plateau. *Advances in Atmospheric Sciences*, *29*(5), 978–992. https://doi.org/10.1007/s00376-012-1220-y

Duine, G. J., Carvalho, L. M. V., Jones, C., & Zigner, K. (2021). The effect of upstream orography on the onset of sundowner winds in coastal Santa Barbara, CA. *Journal of Geophysical Research: Atmospheres*, *126*(8), e2020JD033791. https://doi.org/10.1029/2020jd033791

ECMWF. (2011). The ECMWF reanalysis-interim (ERA-Interim) [Dataset]. *ECMWF*. Retrieved from https://www.ecmwf.int/en/forecasts/dataset/ecmwf-reanalysis-interim

ECMWF. (2019). The land component of the ECMWF reanalysis version 5 (ERA5-Land) [Dataset]. *ECMWF*. Retrieved from https://www.ecmwf.int/en/forecasts/dataset/era5-land

ECMWF. (2020). The ECMWF reanalysis version 5 (ERA5) [Dataset]. *ECMWF*. Retrieved from https://www.ecmwf.int/en/forecasts/dataset/ecmwf-reanalysis-v5

Gao, X., & Giorgi, F. (2017). Use of the RegCM system over East Asia: Review and perspectives. *Engineering*, *3*(5), 766–772. https://doi.org/10.1016/J.ENG.2017.05.019

Gao, X., Shi, Y., Han, Z., Wang, M., Wu, J., Zhang, D., et al. (2017). Performance of RegCM4 over major river basins in China. *Advances in Atmospheric Sciences*, *34*(4), 441–455. https://doi.org/10.1007/s00376-016-6179-7

Giorgi, F. (2019). Thirty years of regional climate modeling: Where are we and where are we going next? *Journal of Geophysical Research: Atmospheres*, *124*(11), 5696–5723. https://doi.org/10.1029/2018jd030094

Giorgi, F., Coppola, E., Solmon, F., Mariotti, L., Sylla, M., Bi, X., et al. (2012). RegCM4: Model description and preliminary tests over multiple CORDEX domains. *Climate Research*, *52*, 7–29. https://doi.org/10.3354/cr01018

Grabowski, W. W. (1989). On the influence of small-scale topography on precipitation. *Quarterly Journal of the Royal Meteorological Society*, *115*(487), 633–650. https://doi.org/10.1002/qj.49711548711

Gu, C., Huang, A., Li, X., Yang, B., Zhou, X., & Wu, Y. (2023a). The source codes of sub-grid turbulent orographic form drag parameterization scheme suitable for the regional climate model version 4.5.0 (RegCM4) [Software]. *Zenodo*. https://doi.org/10.5281/zenodo.8077329

Gu, C., Huang, A., Li, X., Yang, B., Zhou, X., & Wu, Y. (2023b). Impact of sub-grid turbulent orographic form drag on the summer monsoon precipitation simulation over China. *Journal of Geophysical Research: Atmospheres*, *128*(20), e2023JD039113. https://doi.org/10.1029/2023jd039113

Hersbach, H., Bell, B., Berrisford, P., Hirahara, S., Horányi, A., Muñoz-Sabater, J., et al. (2020). The ERA5 global reanalysis. *Quarterly Journal of the Royal Meteorological Society*, *146*(730), 1999–2049. https://doi.org/10.1002/qj.3803

Holtslag, A. A. M., De Bruijn, E. I. F., & Pan, H.-L. (1990). A high resolution air mass transformation model for short-range weather forecasting. *Monthly Weather Review*, *118*(8), 1561–1575. https://doi.org/10.1175/1520-0493(1990)118<1561:Ahramt>2.0.Co;2

Huang, R., Chen, J., & Huang, G. (2007). Characteristics and variations of the East Asian monsoon system and its impacts on climate disasters in China. *Advances in Atmospheric Sciences*, *24*(6), 993–1023. https://doi.org/10.1007/s00376-007-0993-x

ICTP. (2016). The regional climate model version 4.5.0 (RegCM4) [Software]. *Zenodo*. https://doi.org/10.5281/zenodo.8077329

Jiménez, P. A., & Dudhia, J. (2012). Improving the representation of resolved and unresolved topographic effects on surface wind in the WRF model. *Journal of Applied Meteorology and Climatology*, *51*(2), 300–316. https://doi.org/10.1175/JAMC-D-11-084.1

Jin, D., & Huo, L. (2018). Influence of tropical Atlantic sea surface temperature anomalies on the East Asian summer monsoon. *Quarterly Journal of the Royal Meteorological Society*, *144*(714), 1490–1500. https://doi.org/10.1002/qj.3296

Kain, J. S., & Fritsch, J. M. (1990). A one-dimensional entraining/detraining plume model and its application in convective parameterization. *Journal of the Atmospheric Sciences*, *47*(23), 2784–2802. https://doi.org/10.1175/1520-0469(1990)047<2784:AODEPM>2.0.CO;2

Kiehl, J. T., Hack, J. J., Bonan, G. B., Boville, B. A., Williamson, D. L., & Rasch, P. J. (1998). The national center for atmospheric research community climate model: CCM3. *Journal of Climate*, *11*(6), 1131–1149. https://doi.org/10.1175/1520-0442(1998)011<1131:Tncfar>2.0.Co;2

Kim, Y. J., Eckermann, S. D., & Chun, H. Y. (2003). An overview of the past, present and future of gravity-wave drag parametrization for numerical climate and weather prediction models. *Atmosphere-Ocean*, *41*(1), 65–98. https://doi.org/10.3137/ao.410105

Kong, W., & Chiang, J. C. H. (2020). Interaction of the westerlies with the Tibetan Plateau in determining the Mei-Yu termination. *Journal of Climate*, *33*(1), 339–363. https://doi.org/10.1175/JCLI-D-19-0319.1

Koo, M. S., Choi, H. J., & Han, J. Y. (2018). A parameterization of turbulent-scale and mesoscale orographic drag in a global atmospheric model. *Journal of Geophysical Research: Atmospheres*, *123*(16), 8400–8417. https://doi.org/10.1029/2017JD028176

Krishnamurti, T. N., & Surgi, N. (1987). Observational aspects of the summer monsoon.

Lane, T. P., & Watson, C. D. (2012). Sensitivities of orographic precipitation to terrain geometry and upstream conditions in idealized simulations. *Journal of the Atmospheric Sciences*, *69*(4), 1208–1231. https://doi.org/10.1175/jas-d-11-0198.1

Li, B., Zhou, L., Qin, J., & Meng, Z. (2022). Maintenance of cyclonic vortex during monsoon intraseasonal oscillation: A view from kinetic energy budget. *Geophysical Research Letters*, *49*(7), e2022GL097740. https://doi.org/10.1029/2022GL097740

Li, J., Geen, R., Mao, J., Song, Y., Vallis, G. K., & Wu, G. (2023a). Mechanical and thermal forcings of Asian large-scale orography on spring cloud amount and atmospheric radiation budget over East Asia. *Journal of Climate*, *36*(15), 1–37. https://doi.org/10.1175/JCLI-D-22-0797.1

Li, S., Sato, T., Nakamura, T., & Guo, W. (2023b). East Asian summer rainfall stimulated by subseasonal Indian monsoonal heating. *Nature Communications*, *14*(1), 5932. https://doi.org/10.1038/s41467-023-41644-5

Liang, Y., Wang, L., Zhang, G. J., & Wu, Q. (2017). Sensitivity test of parameterizations of subgrid-scale orographic form drag in the NCAR CESM1. *Climate Dynamics*, *48*(9), 3365–3379. https://doi.org/10.1007/s00382-016-3272-7

Lim, K. S. S., Lim, J. M., Shin, H. H., Hong, J., Ji, Y. Y., & Lee, W. (2019). Impacts of subgrid-scale orography parameterization on simulated atmospheric fields over Korea using a high-resolution atmospheric forecast model. *Meteorology and Atmospheric Physics*, *131*(4), 975–985. https://doi.org/10.1007/s00703-018-0615-4

Liu, K., Yu, F., Su, Y., Zhang, H., Chen, Q., & Sun, J. (2023). Improved gravity wave drag to enhance precipitation simulation: A case study of typhoon in-fa. *Atmosphere*, *14*(12), 1801. https://doi.org/10.3390/atmos14121801

Lu, M., Yang, S., Wang, J., Wu, Y., & Jia, X. (2021). Response of regional Asian summer monsoons to the effect of reduced surface Albedo in different Tibetan plateau domains in idealized model experiments. *Journal of Climate*, 1–49. https://doi.org/10.1175/jcli-d-20-0500.1

Matsukawa, C., Kuroki, Y., & Kanehama, T. (2022). Optimization of orographic drag parametrizations in the JMA operational global model using COORDE-type experiments. *WGNE Res. Activ. Earth Sys. Modell*.

Milton, S. F., & Wilson, C. A. (1996). The impact of parameterized subgrid-scale orographic forcing on systematic errors in a global NWP model. *Monthly Weather Review*, *124*(9), 2023–2045. https://doi.org/10.1175/1520-0493(1996)124<2023:TIOPSS>2.0.CO;2

Muñoz-Sabater, J. (2019). ERA5-Land hourly data from 1950 to present. *Copernicus Climate Change Service (C3S) Climate Data Store (CDS)*. https://doi.org/10.24381/cds.e2161bac

NOAA. (2002). The weekly NOAA optimum interpolation sea surface temperature (OISST) [Dataset]. *National Oceanic and Atmospheric Administration*. Retrieved from https://psl.noaa.gov/data/gridded/data.noaa.oisst.v2.html

Oleson, K., Lawrence, D., Bonan, G., Drewniak, B., Huang, M., Koven, C., et al. (2010). Technical description of version 4.5 of the community land model (CLM), NCAR Tech. *Notes (NCAR/TN-478+ STR)*, 605.

Pal, J. S., Small, E. E., & Eltahir, E. A. B. (2000). Simulation of regional-scale water and energy budgets: Representation of subgrid cloud and precipitation processes within RegCM. *Journal of Geophysical Research*, *105*(D24), 29579–29594. https://doi.org/10.1029/2000JD900415

Pepler, A., Dowdy, A., & Hope, P. (2018). A global climatology of surface anticyclones, their variability, associated drivers and long-term trends. *Climate Dynamics*, *52*(9–10), 5397–5412. https://doi.org/10.1007/s00382-018-4451-5

Pontoppidan, M., Reuder, J., Mayer, S., & Kolstad, E. W. (2017). Downscaling an intense precipitation event in complex terrain: The importance of high grid resolution. *Tellus A: Dynamic Meteorology and Oceanography*, *69*(1), 1271561. https://doi.org/10.1080/16000870.2016.1271561

Raju, P., Bhatla, R., Almazroui, M., & Assiri, M. (2015). Performance of convection schemes on the simulation of summer monsoon features over the South Asia CORDEX domain using RegCM-4.3. *International Journal of Climatology*, *35*(15), 4695–4706. https://doi.org/10.1002/joc.4317

Ren, H. C., Li, W., Ren, H. L., & Zuo, J. (2016). Distinct linkage between winter Tibetan Plateau snow depth and early summer Philippine Sea anomalous anticyclone. *Atmospheric Science Letters*, *17*(3), 223–229. https://doi.org/10.1002/asl.646

Reynolds, R. W., Rayner, N. A., Smith, T. M., Stokes, D. C., & Wang, W. (2002). An improved in situ and satellite SST analysis for climate. *Journal of Climate*, *15*(13), 1609–1625. https://doi.org/10.1175/1520-0442(2002)015<1609:AIISAS>2.0.CO;2

Ronghui, H., & Yifang, W. (1989). The influence of ENSO on the summer climate change in China and its mechanism. *Advances in Atmospheric Sciences*, *6*(1), 21–32. https://doi.org/10.1007/BF02656915

Rontu, L. (2006). A study on parametrization of orography-related momentum fluxes in a synoptic-scale NWP model. *Tellus Series a-Dynamic Meteorology and Oceanography*, *58*(1), 69–81. https://doi.org/10.1111/j.1600-0870.2006.00162.x

Sanders, F. (1988). Life history of mobile troughs in the upper westerlies. *Monthly Weather Review*, *116*(12), 2629–2648. https://doi.org/10.1175/1520-0493(1988)116<2629:LHOMTI>2.0.CO;2

Seok, S.-H., & Seo, K.-H. (2021). Sensitivity of East Asian summer monsoon precipitation to the location of the Tibetan Plateau. *Journal of Climate*, *34*(22), 8829–8840. https://doi.org/10.1175/JCLI-D-21-0154.1

Shalaby, A., Zakey, A., Tawfik, A., Solmon, F., Giorgi, F., Stordal, F., et al. (2012). Implementation and evaluation of online gas-phase chemistry within a regional climate model (RegCM-CHEM4). *Geoscientific Model Development*, *5*(3), 741–760. https://doi.org/10.5194/gmd-5-741-2012

Shi, X., Wang, Y., & Xu, X. (2008). Effect of mesoscale topography over the Tibetan Plateau on summer precipitation in China: A regional model study. *Geophysical Research Letters*, *35*(19), L19707. https://doi.org/10.1029/2008GL034740

Shi, Z., Sha, Y., & Liu, X. (2017). Effect of Yunnan–Guizhou topography at the southeastern Tibetan Plateau on the Indian monsoon. *Journal of Climate*, *30*(4), 1259–1272. https://doi.org/10.1175/jcli-d-16-0105.1

Sikka, D., & Narasimha, R. (1995). Genesis of the monsoon trough boundary layer experiment (MONTBLEX). *Proceedings of the Indian Academy of Sciences - Earth & Planetary Sciences*, *104*(2), 157–187. https://doi.org/10.1007/BF02839270

Son, J. H., Seo, K. H., & Wang, B. (2020). How does the Tibetan plateau dynamically affect downstream monsoon precipitation? *Geophysical Research Letters*, *47*(23), e2020GL090543. https://doi.org/10.1029/2020gl090543

Student. (1908). The probable error of a mean. *Biometrika*, *6*(1), 1–25. https://doi.org/10.2307/2331554

Tao, F., Yokozawa, M., Zhang, Z., Hayashi, Y., Grassl, H., & Fu, C. (2004). Variability in climatology and agricultural production in China in association with the east Asian summer monsoon and El Niño southern oscillation. *Climate Research*, *28*(1), 23–30. https://doi.org/10.3354/cr028023

Tiedtke, M. (1996). An extension of cloud-radiation parameterization in the ECMWF model: The representation of subgrid-scale variations of optical depth. *Monthly Weather Review*, *124*(4), 745–750. https://doi.org/10.1175/1520-0493(1996)124<0745:Aeocrp>2.0.Co;2

Van Den Dool, H. M. (1987). An empirical study on the parameterization of precipitation in a model of the time mean atmosphere. *Journal of the Atmospheric Sciences*, *44*(1), 224–235. https://doi.org/10.1175/1520-0469(1987)044<0224:AESOTP>2.0.CO;2

Van Niekerk, A., Sandu, I., & Vosper, S. B. (2018). The circulation response to resolved versus parametrized orographic drag over complex mountain terrains. *Journal of Advances in Modeling Earth Systems*, *10*(10), 2527–2547. https://doi.org/10.1029/2018MS001417

Wang, Y., Yang, K., Zhou, X., Chen, D. L., Lu, H., Ouyang, L., et al. (2020). Synergy of orographic drag parameterization and high resolution greatly reduces biases of WRF-simulated precipitation in central Himalaya. *Climate Dynamics*, *54*(3–4), 1729–1740. https://doi.org/10.1007/s00382-019-05080-w

Wei, W., Zhang, R., Wen, M., Rong, X., & Li, T. (2014). Impact of Indian summer monsoon on the South Asian High and its influence on summer rainfall over China. *Climate Dynamics*, *43*(5–6), 1257–1269. https://doi.org/10.1007/s00382-013-1938-y

Weng, H., Ashok, K., Behera, S. K., Rao, S. A., & Yamagata, T. (2007). Impacts of recent El Niño Modoki on dry/wet conditions in the Pacific rim during boreal summer. *Climate Dynamics*, *29*(2–3), 113–129. https://doi.org/10.1007/s00382-007-0234-0

Wood, N., Brown, A. R., & Hewer, F. E. (2001). Parametrizing the effects of orography on the boundary layer: An alternative to effective roughness lengths. *Quarterly Journal of the Royal Meteorological Society*, *127*(573), 759–777. https://doi.org/10.1256/smsqj.57302

Wu, G., Duan, A., Liu, Y., Mao, J., Ren, R., Bao, Q., et al. (2014). Tibetan Plateau climate dynamics: Recent research progress and outlook. *National Science Review*, *2*(1), 100–116. https://doi.org/10.1093/nsr/nwu045

Wu, G., Zhuo, H., Wang, Z., & Liu, Y. (2016). Two types of summertime heating over the Asian large-scale orography and excitation of potential-vorticity forcing I. Over Tibetan Plateau. *Science China Earth Sciences*, *59*(10), 1996–2008. https://doi.org/10.1007/s11430-016-5328-2

Wu, Z., Wang, B., Li, J., & Jin, F. F. (2009). An empirical seasonal prediction model of the East Asian summer monsoon using ENSO and NAO. *Journal of Geophysical Research*, *114*(D18), D18120. https://doi.org/10.1029/2009JD011733

Xu, X., Huang, A., Huang, Q., Zhang, Y., Wu, Y., Gu, C., et al. (2022). Impacts of horizontal resolution of the lateral boundary conditions and downscaling method on the performance of RegCM4. 6 in simulating the surface climate over central-eastern China. *Earth and Space Science*, *9*(8), e2022EA002433. https://doi.org/10.1029/2022EA002433

Xu, X., Huang, A., Zhao, W., Yang, B., Xue, D., & Zhang, Y. (2024). Roles of the Tibetan Plateau and Yunnan-Guizhou Plateau in the regional extreme precipitation over sichuan basin in summer: A case study. *Journal of Geophysical Research: Atmospheres*, *129*(3), e2023JD039776. https://doi.org/10.1029/2023JD039776

Xue, H., & Shen, X. (2023). A turbulent orographic form drag scheme accounting for anisotropy and orientation for kilometer-to subkilometer-scale models. *Quarterly Journal of the Royal Meteorological Society*, *149*(755), 2527–2549. https://doi.org/10.1002/qj.4519

Xue, H., Shen, X. S., & Su, Y. (2011). Parameterization of turbulent orographic form drag and implementation in GRAPES. *Journal of Applied Meteorological Science*, *22*(2), 169–181. https://doi.org/10.3969/j.issn.1001-7313.2011.02.006

Xue, H., Zhou, X., Luo, Y., & Yin, J. (2021). Impact of parameterizing the turbulent orographic form drag on convection-permitting simulations of winds and precipitation over South China during the 2019 pre-summer rainy season. *Atmospheric Research*, *263*, 105814. https://doi.org/10.1016/j.atmosres.2021.105814

Yatagai, A., Kamiguchi, K., Arakawa, O., Hamada, A., Yasutomi, N., & Kitoh, A. (2012). APHRODITE: Constructing a long-term daily gridded precipitation dataset for asia based on a dense network of rain gauges. *Bulletin of the American Meteorological Society*, *93*(9), 1401–1415. https://doi.org/10.1175/bams-d-11-00122.1

Ye, H., & Lu, R. (2012). Dominant patterns of summer rainfall anomalies in East China during 1951–2006. *Advances in Atmospheric Sciences*, *29*(4), 695–704. https://doi.org/10.1007/s00376-012-1153-5

Yim, S. Y., Jhun, J. G., Lu, R., & Wang, B. (2010). Two distinct patterns of spring Eurasian snow cover anomaly and their impacts on the East Asian summer monsoon. *Journal of Geophysical Research*, *115*(D22), D22113. https://doi.org/10.1029/2010JD013996

Zeng, X., Zhao, M., & Dickinson, R. E. (1998). Intercomparison of bulk aerodynamic algorithms for the computation of sea surface fluxes using TOGA COARE, and TAO data. *Journal of Climate*, *11*(10), 2628–2644. https://doi.org/10.1175/1520-0442(1998)011<2628:Iobaaf>2.0.Co;2

Zhang, R., Xu, X., & Wang, Y. (2020). Impacts of subgrid orographic drag on the summer monsoon circulation and precipitation in East Asia. *Journal of Geophysical Research: Atmospheres*, *125*(13), e2019JD032337. https://doi.org/10.1029/2019JD032337

Zheng, J., Wang, W.-C., Ge, Q., Man, Z., & Zhang, P. (2006). Precipitation variability and extreme events in eastern China during the past 1500 years. *TAO: Terrestrial, Atmospheric and Oceanic Sciences*, *17*(3), 579. https://doi.org/10.3319/tao.2006.17.3.579(a)

Zhou, X., Beljaars, A., Wang, Y., Huang, B., Lin, C., Chen, Y., & Wu, H. (2017). Evaluation of WRF simulations with different selections of subgrid orographic drag over the Tibetan Plateau. *Journal of Geophysical Research: Atmospheres*, *122*(18), 9759–9772. https://doi.org/10.1002/2017JD027212

Zhou, X., Yang, K., Beljaars, A., Li, H. D., Lin, C. G., Huang, B., & Wang, Y. (2019). Dynamical impact of parameterized turbulent orographic form drag on the simulation of winter precipitation over the western Tibetan Plateau. *Climate Dynamics*, *53*(1–2), 707–720. https://doi.org/10.1007/s00382-019-04628-0

Zhou, X., Yang, K., & Wang, Y. (2017). Implementation of a turbulent orographic form drag scheme in WRF and its application to the Tibetan Plateau. *Climate Dynamics*, *50*(7–8), 2443–2455. https://doi.org/10.1007/s00382-017-3677-y

Zhuang, M., Duan, A., Lu, R., Li, P., & Yao, J. (2022). Relative impacts of the orography and land–sea contrast over the Indochina Peninsula on the Asian summer monsoon between early and late summer. *Journal of Climate*, *35*(10), 3037–3055. https://doi.org/10.1175/JCLI-D-21-0576.1